JOURNAL OF PETROLOGY | VOLUME 49 | NUMBER 10 | PAGES 1755–1780 | 2008 | doi:10.1093/petrology/egn045

Multiple Plagioclase Crystal Populations Identified by Crystal Size Distribution and *in situ* Chemical Data: Implications for Timescales of Magma Chamber Processes Associated with the 1915 Eruption of Lassen Peak, CA

MORGAN J. SALISBURY[1]*, WENDY A. BOHRSON[1†], MICHAEL A. CLYNNE[2], FRANK C. RAMOS[3] AND PAUL HOSKIN[4]

[1]DEPARTMENT OF GEOLOGICAL SCIENCES, CENTRAL WASHINGTON UNIVERSITY, ELLENSBURG, WA 98926, USA

[2]US GEOLOGICAL SURVEY, 345 MIDDLEFIELD ROAD, MENLO PARK, CA 94025, USA

[3]DEPARTMENT OF GEOLOGICAL SCIENCES, NEW MEXICO STATE UNIVERSITY, LAS CRUCES, NM 88003, USA

[4]DEPARTMENT OF GEOSCIENCE, UNIVERSITY OF CALGARY, CALGARY, ALBERTA T2N 1N4, CANADA

RECEIVED DECEMBER 20, 2007; ACCEPTED SEPTEMBER 2, 2008
ADVANCE ACCESS PUBLICATION OCTOBER 10, 2008

Products of the 1915 Lassen Peak eruption reveal evidence for a magma recharge–magma mixing event that may have catalyzed the eruption and from which four compositional members were identified: light dacite, black dacite, andesitic inclusion, and dark andesite. Crystal size distribution, textural, and in situ chemical (major and trace element and Sr isotope) data for plagioclase from these compositional products define three crystal populations that have distinct origins: phenocrysts (long axis > 0·5 mm) that typically have core An contents between 34 and 36 mol %, microphenocrysts (long axis between 0·1 and 0·5 mm) that have core An contents of 66–69, and microlites (long axis < 0·1 mm) with variable An core contents from 64 to 52. Phenocrysts are interpreted to form in an isolated dacitic magma chamber that experienced slow cooling. Based on textural, compositional, and isotopic data for the magma represented by the dacitic component, magma recharge was not an important process until just prior to the 1915 eruption. Average residence times for phenocrysts are in the range of centuries to millennia. Microphenocrysts formed in a hybrid layer that resulted from mixing between end-member reservoir dacite and recharge magma of basaltic andesite composition. High thermal contrast between the two end-member magmas led to relatively high degrees of undercooling, which resulted in faster crystal growth rates and acicular and swallowtail crystal habits. Some plagioclase phenocrysts from the dacitic chamber were incorporated into the hybrid layer and underwent dissolution–precipitation, seen in both crystal textures and rim compositions. Average microphenocryst residence times are of the order of months. Microlites may have formed in response to decompression and/or syn-eruptive degassing as magma ascended from the chamber through the volcanic conduit. Chemical distinctions in plagioclase microlite An contents reveal that melt of the dark andesite was more mafic than the melt of the other three compositions. We suggest that mixing of an intruding basaltic andesite and reservoir dacite before magma began ascending in the conduit allowed formation of a compositionally distinct microlite population. Melt in the other three products was more evolved because it had undergone differentiation during the months following initial mixing; as a consequence, melt and microlites among these three products have similar compositions. The results of this study highlight the integrated use of crystal size distribution, textural, and in situ chemical data in identifying distinct crystal populations and linking these populations to the thermal and chemical characteristics of complex magma bodies.

KEY WORDS: *crystal size distribution; Lassen Peak; magma mixing; timescale;* in situ

*Present address: Department of Geosciences, Oregon State University, Corvallis, OR 97331, USA.
†Corresponding author. Telephone: 509.963.2835. Fax: 509.963.2821. E-mail: bohrson@geology.cwu.edu

© The Author 2008. Published by Oxford University Press. All rights reserved. For Permissions, please e-mail: journals.permissions@oxfordjournals.org

INTRODUCTION

Mixing of thermally and compositionally distinct magmas leads to a diverse array of whole-rock characteristics, mineral and rock textures, and mineral zoning, and also has the potential to influence eruption dynamics. Evidence for magma mixing, which ranges from macroscale banding in erupted products (e.g. banded pumice of the 1915 Lassen Peak eruption, Clynne, 1999) to micro-scale disequilibrium textures and compositional zoning (e.g. Nakamura, 1995; Tepley *et al.*, 1999; Browne *et al.*, 2006), provides constraints for numerous models describing the spectrum of possible mixing or mingling mechanisms.

Particularly in the case of intermediate composition magmas, the typical products of magma mixing are basaltic to andesitic inclusions that are found in dacitic to rhyolitic volcanic products but are also important components in evolved plutonic bodies (Eichelberger, 1980; Bacon, 1986). These inclusions are commonly fine-grained, ellipsoidal blobs that have high vesicle contents and disequilibrium crystal assemblages (i.e. compositional and textural evidence of disequilibrium) (e.g. Eichelberger, 1980; Bacon, 1986). The combined textural and chemical characteristics of these inclusions have led to a formation model involving injection of hotter, more mafic magma into a cooler, more silicic body. Depending on volume and temperature contrasts, the mafic magma may mix with the more silicic magma, producing a hybrid magma (Sparks & Marshall, 1986). The key aspect of this interaction is that cooling of the more mafic material enhances crystallization, which in turn may cause volatile saturation, exsolution and formation of a mafic foam. This foam is typically less dense than the host silicic magma, producing possible instabilities in the magma body. In some cases, these instabilities may catalyze a volcanic eruption (Eichelberger, 1980). Such a cause–effect relationship has important implications for volcanic hazard assessment, particularly if the mixing event can be detected through seismic and/or other means of active monitoring and if a characteristic timescale between the mixing event and eruption can be defined.

Recent advances in *in situ* chemical analysis techniques have permitted the study of mixed magma products at a range of scales. These data, coupled with textural information, have led to better insights into processes of magma mixing (Singer *et al.*, 1995; Pallister *et al.*, 1996; Tepley *et al.* 1999; Coombs *et al.* 2000; Izbekov *et al.*, 2004; Browne *et al.*, 2006). Documenting timescales of mixing requires knowledge of time-dependent parameters such as diffusion or crystal growth. Theory developed for crystal size distributions (CSDs, e.g. Randolf & Larson, 1971; Cashman & Marsh, 1988; Marsh, 1988, 1998; Higgins, 2000, 2006) provides a method for determining the average residence time for a population of crystals by equating the slope of a CSD to $-1/(\text{growth rate} \times \text{residence time})$. This method has been used to determine timescales of magmatic processes in a variety of volcanic settings (e.g. Mangan, 1990; Resmini & Marsh, 1995; Higgins, 1996*a*, 1996*b*). The well-documented relationship between rock texture, as manifested by crystal size data, and cooling history provides potentially valuable information about the thermal conditions of a magma body (Cashman, 1993).

As documented by Clynne (1999), the 1915 Lassen Peak (USA) eruption produced four volcanic products interpreted to result from a magma mixing event. In this study, we combine CSD data, Nomarski differential interference contrast (NDIC) images, and *in situ* major and trace element and isotopic data from plagioclase in the four products to further constrain how and over what timescales magma mixing occurred. Such integration allows plagioclase in the four products to be divided into distinct populations, each with a unique origin and timescale of formation.

BACKGROUND

Geological setting of Lassen Peak volcano and chronology of the 1915 eruption

Lassen Peak volcano, the southernmost of the Cascade volcanoes, lies within the Lassen Volcanic Center (LVC) in northeastern California (Fig. 1). The LVC is situated above the subducting Gorda plate and lies on the western edge of the Basin and Range province; both of these tectonic regimes contribute to volcanism in the region (Guffanti *et al.*, 1990). The LVC is the youngest of five volcanic centers that have been active in the Lassen Volcanic National Park region during the past 3 Myr (Clynne, 1990). Lassen Peak volcano is the highest and largest of a group of more than 30 domes that have been emplaced over the past 300 kyr (Clynne *et al.*, 1999). The Lassen Peak dome formed in a single, silicic eruption at about 27 ka (Turrin *et al.*, 1998), and no additional activity occurred until 1915. Nearby Chaos Crags erupted at 1·1 ka (Clynne, 1999). Evidence of magma mixing, including disequilibrium phenocryst assemblages and undercooled mafic inclusions, is common in the LVC, including the 27 ka eruption of Lassen Peak (Turrin *et al.*, 1998) and the 1·1 ka eruption of Chaos Crags (Tepley *et al.*, 1999).

Activity related to the 1915 eruption of Lassen Peak began on May 30, 1914, and numerous steam explosions persisted until lava erupted in mid-May 1915. Within a week, four distinct rock types, as identified by Clynne (1999), erupted from the summit: (1) black dacite containing (2) undercooled andesitic inclusions, (3) compositionally banded pumice with dark andesite and light dacite bands, and (4) unbanded light dacite. The black dacite began to erupt and form a dome on May 14, 1915. The growing dome of black dacite was disrupted on May 19 by a phreatic explosion that unplugged the vent and black

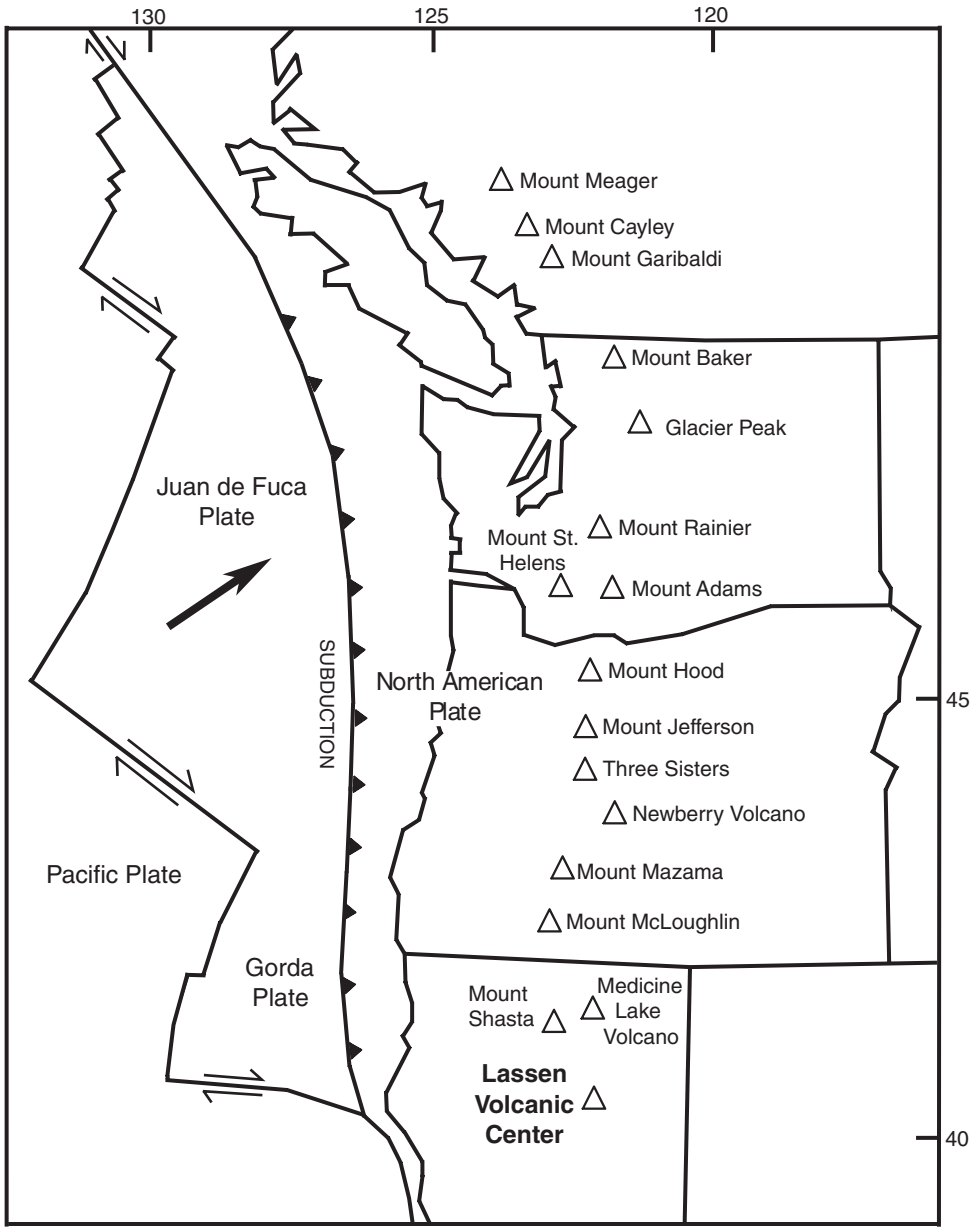

Fig. 1. Tectonic setting of major volcanic centers of the Cascadia subduction zone including Lassen Peak.

dacite magma flowed down the western and northeastern flanks on May 19 and 20. Following two quiet days, a subplinian eruption on May 22 produced banded light dacite and dark andesite pumice, and as the eruption progressed, unbanded light dacite pumice (Clynne, 1999). The sequence of events and distribution of products of the 1915 eruption has been further documented by Christiansen *et al.* (2002).

Descriptions of 1915 Lassen Peak rock types

Below is a summary of relevant information from Clynne (1999), focusing mainly on plagioclase. For a detailed review of the lithology and mineralogy of the 1915 rocks, readers are directed to that study. The present study focuses on plagioclase because of its high modal abundance and relatively slow rate of re-equilibration, which allows preservation of a record of complex magmatic processes (e.g. Pearce & Kolisnik, 1990; Singer *et al.*, 1995; Tepley *et al.*, 1999) such as magma mixing.

The black dacite (64–65 wt % SiO_2) is a microvesicular, glassy, porphyritic rock containing 20–25% plagioclase phenocrysts (up to 5 mm), of which *c.* 20–30% display significant zones with reaction characteristics. Reacted zones are marked by small glass inclusions and are commonly

described by such textural terms as sieved, mottled, mantled, cloudy or dusty. These textures probably result from partial dissolution of plagioclase as a reaction to hotter magmas associated with magma mixing (Tsuchiyama & Takahashi, 1983). The black dacite also contains phenocrysts of biotite, hornblende, quartz, and olivine, and microphenocrysts of plagioclase, clinopyroxene, orthopyroxene, olivine, and titanomagnetite. The black dacite contains abundant (~5%) undercooled andesitic inclusions (57–59·5 wt % SiO_2) that range up to ~50 cm in diameter and are typically subrounded to subangular. Morphologically and texturally similar inclusions, also known as mafic inclusions or enclaves, have been described at a number of subduction-related volcanoes (e.g. Bacon, 1986; Thomas & Tait, 1997; Coombs *et al.*, 2002) and are attributed to mixing between magmas of different composition and temperature. In these inclusions, phenocrysts of plagioclase, olivine, hornblende, biotite, titanomagnetite, and quartz are set in a microvesicular groundmass composed of ~50% interstitial glass, ~30% microphenocrysts of plagioclase (commonly swallow-tailed or hollow-textured), and lesser amounts of clinopyroxene and orthopyroxene. All plagioclase phenocrysts in the inclusions exhibit reaction characteristics. Andesitic inclusions are absent in unmixed dark andesite and are rare in the light dacite.

Light dacite is microvesicular to pumiceous, has the same phenocryst assemblage as the black dacite, and has similar to higher SiO_2 (64·5–68 wt %). The most silicic light dacite is less porphyritic and has fewer reacted plagioclase phenocrysts than the black dacite. The least silicic is very similar in composition to the black dacite. Dark andesite (60–61 wt % SiO_2) is a glassy, microvesicular to pumiceous rock with olivine phenocrysts, pyroxene, and plagioclase microphenocrysts, and rare reacted plagioclase phenocrysts.

Typically, unreacted plagioclase phenocrysts are relatively clear and characterized by oscillatory zoning. Compositions near An_{30} are typical, but cores up to An_{45} have been documented in addition to rare, ragged xenocrystic cores as calcic as An_{80} (Clynne, 1999). More calcic rims are common (up to An_{50}), more so in the black dacite compared with the light dacite. Reacted crystals have overgrowth rims up to 0·10 mm thick that are more calcic (An_{75}) and exhibit strong normal zoning to the crystal edge (An_{50}). Acicular plagioclase microphenocrysts up to 0·5 mm are most abundant in the andesitic inclusions, common in the black and light dacite, and sparse in the dark andesite. Cores of the microphenocrysts are in the range of An_{75}, but the crystals are strongly normally zoned to An_{50} at the rims.

Lassen Peak magma mixing model

Compositional diversity, disequilibrium phenocryst assemblages and reacted plagioclase phenocrysts in the 1915 products led Clynne (1999) to develop a model of mixing between intruding basaltic andesite and a reservoir dacitic magma containing unreacted plagioclase, biotite, amphibole, orthopyroxene, quartz, and titanomagnetite. Mineralogy and mixing calculations indicated that the intruding magma was probably a basaltic andesite. Consistent with a magma mixing hypothesis, a conspicuous feature of the 1915 Lassen Peak eruption products is the presence of andesitic inclusions.

Turbulent mixing between the two thermally and compositionally distinct magmas formed a hybrid andesitic magma. Heat loss from the hybrid magma to the overlying dacite resulted in undercooling, which led to rapid crystallization of new plagioclase microphenocrysts, resulting in supersaturation of volatiles and the creation of a layer of mafic foam. The highly vesicular hybrid magma then partially broke up and rose into the host dacite forming microphenocryst-rich andesitic inclusions. Disaggregation of some of these andesitic inclusions into the host dacite generated the black dacite. When the black dacite could no longer cool the hybrid mafic magma to the point of vesiculation, mixing occurred between the mafic magma and the black dacite, producing the dark andesite magma. Ascent and eruption of the hot, volatile-rich black dacite allowed the dark andesite and light dacite to mix in the conduit *en route* to the surface, ultimately forming banded pumice.

DESCRIPTION OF SAMPLES, DATA COLLECTION AND ANALYTICAL PROCEDURES

A representative sample of each of the four compositional types (black dacite, light dacite, andesitic inclusion, dark andesite) identified by Clynne (1999) was collected for detailed analysis. For each sample, one 100 μm thick doubly polished section was produced. From each section, plagioclase crystals were analyzed for four types of data: (1) crystal size distribution (CSD); (2) detailed textural information from Nomarksi differential image contrast (NDIC) imaging (Anderson, 1983; Pearce & Clark, 1989; Tepley *et al.*, 1999); (3) *in situ* major and trace element concentrations; (4) *in situ* Sr isotope ratios.

An important aspect of this study is the integration of data from each of these techniques. To correlate plagioclase compositional and textural information with size, the location of each crystal analyzed was recorded by assigning an address (x, y coordinate) to each crystal on digital images of polished sections. These images were obtained by aluminum X-ray analysis using the Oregon State University CAMECA SX-50 electron-microprobe (Fig. 2). Plagioclase was effectively resolved on the images because of the abundance of aluminum in the crystals. For each sample, aluminum X-ray images were obtained at two scales to effectively resolve both smaller and larger crystals (Fig. 2a and b).

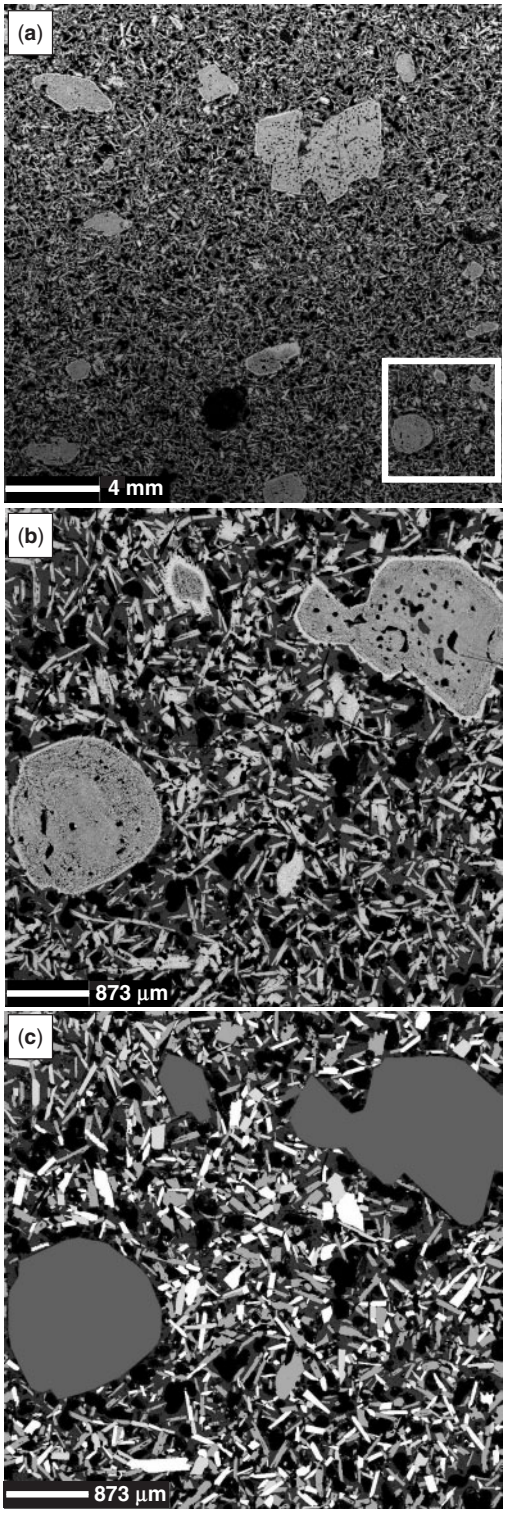

Fig. 2. (a) Al intensity X-ray map (20 × 20 mm; 1024 × 1024 pixels) used to define plagioclase phenocryst numbers and geometry within the andesitic inclusion. The image was obtained with the electron microprobe using wavelength-dispersive spectrometers, a fixed electron beam, and a scanning stage. Run conditions included a 100 nA beam current with a 1 μm diameter beam and a dwell time of 15 ms/pixel. Box shows approximate location of (b) and (c). (b) Al intensity image (5 × 5 mm; 1024 × 1024 pixels) of andesite inclusion. (c) Processed image of (b) showing plagioclase crystals outlined automatically from Al X-ray map using Adobe Photoshop. Crystals with common edges or points were manually outlined and assigned a different color for recognition within NIH Image. Details of the procedure have been given by Salisbury (2003).

Two-dimensional (2D), long-axis crystal lengths and area measurements of plagioclase crystals were made from the X-ray images using National Institute of Health software (NIH Image 1.62). Plagioclase crystals were outlined manually using Adobe Photoshop and assigned a solid color prior to NIH Image analysis (Fig. 2c). Boundaries of touching crystals were outlined based on visual inspection of crystal shapes (e.g. Higgins, 2000). Uncertainties introduced by this method were difficult to quantify but are unlikely to significantly affect the size distributions because of the large number of crystals counted ($n = 1194$ to 1849 per sample). In the dacites and andesite, touching crystals make up a very small percentage of the total population (1–3%); however, in the case of the andesitic inclusion, 70–80% of the crystals border at least one other crystal. Measurements from both scales were combined to produce a single CSD for each of the four rock types. Crystals that could be measured in both 5 mm × 5 mm and 20 mm × 20 mm areas produced similar length values, confirming measurement reproducibility between the two scales. Reported CSD data were corrected on a vesicle-free basis. To test the sensitivity of CSD measurements to disequilibrium processes, reacted and unreacted plagioclase phenocrysts were measured separately in the black dacite, which contained a large number of both types of crystal. CSD slopes were similar for reacted and unreacted populations in this unit, thus indicating that no significant bias was introduced by measuring phenocrysts that have potentially been affected by resorption or reaction. Measurement for crystal size was limited to >0·025 mm, below which recognition of crystals became difficult.

CSD analysis was conducted using the 2D long-axis lengths measured in NIH Image from best-fit ellipses that are approximated to each crystal perimeter. Although crystal widths have been used to calculate CSDs (e.g. Garrido *et al.*, 2001), crystal lengths are reported to minimize measurement errors for the smallest crystals and to relate these to published long-axis growth rates. Coombs *et al.* (2002) found good agreement in CSDs from both width and length measurements.

Based on nucleation density, crystal growth rate, and average crystal residence time, a relationship between the natural logarithm of crystal population density vs crystal size can be derived. The population density (n) is calculated numerically as the slope of a cumulative number distribution (N) as a function of size (L), $[n(L) = \mathrm{d}N/\mathrm{d}L]$; thus $n(L)$ is the number of crystals per unit length per

unit volume. Linear least-squares regression of ln (n) vs L was used to calculate the slope and intercept values for CSD data reported in this study. For crystal shapes, no exact transformation from 2D crystal lengths to the third dimension exists; a commonly used conversion from 2D to 3D values raises N to the 3/2 power (e.g. Cashman & Marsh, 1988; Cashman, 1990). Higgins (2000) questioned the use of this conversion on stereological grounds and provided an alternative method to correct for this problem, called *CSDCorrections*.

CSDCorrections requires 2D length measurements, image area, average crystal habit, roundness, and sample foliation. The 3D crystal habits of the plagioclase crystals were estimated from 2D short-axis/long-axis measurements using *CSDslice* software (Morgan & Jerram, 2006). Because *CSDCorrections* cannot, at the time of this writing, input varying shape or rounding estimates for different sets of crystals, all crystals were classified as unrounded, with an average shape of 1:2·1:4·3, based on aspect ratio measurements from *CSDSlice*. All 1915 plagioclase crystals are assumed to be randomly oriented.

Nomarski differential image contrast (NDIC) images were collected at Portland State University. Each 100 μm section was immersed in fluoroboric (HBF_4) acid for 15–30 s. HBF_4 preferentially dissolves Ca-rich zones in plagioclase, thereby producing microtopographic relief of sodic highs and calcic lows. A carbon coat was added to the surface to increase reflectivity and decrease internal reflections within crystals. The relief was imaged by a 35 mm camera using black and white film and a petrographic microscope fitted with Nomarski filters. For each of the four 1915 samples, 15 NDIC images were collected. From these, a detailed textural analysis was carried out on a minimum of 40 crystals per composition.

Based on NDIC textural data, selected crystals were chosen for *in situ* major and trace element analyses. Major elements of plagioclase and glass were analyzed with the Oregon State University CAMECA SX-50 electron microprobe, using an accelerating potential of 15 kV, a beam current of 30 nA, 10 s count times, and a 4 μm diameter spot size. Lake County Labradorite (USNM 115900) and Kakanui Anorthoclase (USNM 133868) were analyzed repeatedly prior to analyses of Lassen Peak plagioclase grains. Major element concentration reproducibility ranges from ≤1% for SiO_2, Na_2O, and Al_2O_3, to ~3·9% for CaO, and ~9·7% for K_2O. Glass analyses were performed using the same calibration procedure and oxide suite as plagioclase and consequently provide a semi-quantitative description.

Trace elements (Sc, Rb, Sr, Y, Ba, La, Ce, Nd, Sm, Eu, Pb) in plagioclase were analyzed by laser ablation inductively coupled plasma mass spectrometry (ICP-MS) at the Australian National University. Instrumentation protocol includes an ArF (193 nm wavelength) Excimer laser, custom-built sample cell and transport system, and HP7500 Agilent ICP-MS system. Ion lens settings were optimized to give large and stable signals across the measured mass range (^{44}Ca to ^{238}U). Signal optimization was performed at the beginning of the analytical session and at regular intervals thereafter during ablation of the reference material NIST SRM 612. Time-resolved spot analyses of three mineral 'unknowns' were bracketed by analyses of NIST SRM 612. Data were standardized using values of NIST SRM 612 from Eggins (2003). For all analyses, Ca from electron microprobe analyses was used as an internal standard for data reduction. Elemental abundances have an estimated uncertainty of ± 15% relative standard deviation. This value combines uncertainties from counting statistics and the size difference of laser ablation pits (75–100 μm diameter) for trace-element analysis and electron microprobe spots (2–5 μm) for major-element determination for external standardization of laser ablation ICP-MS data.

Sr isotope analyses of plagioclase crystals were performed by laser ablation using a New Wave UP213^{TM} Nd YAG laser ablation sampling system and by inductively coupled plasma multiple-collector mass spectrometry (LA-MC-ICPMS) using a ThermoFinniganNeptune^{TM} system and by microdrill sampling at Washington State University. Each reported LA-MC-ICPMS $^{87}Sr/^{86}Sr$ ratio was derived from 30 Sr isotopic ratios measured in 8 s integrations. Laser troughs of 160 μm × 500 μm were used. Laser and MC-ICPMS settings have been reported by Ramos *et al.* (2004). Baselines were measured on-peak for 180 s while flushing the sample chamber with helium, similar to that used during laser sampling. The effects of interfering elements including Yb^{2+}, Er^{2+}, and Rb were accounted for by offline data reduction detailed by Ramos *et al.* (2004). Interference corrected Sr isotope ratios were calculated and exponentially corrected to $^{86}Sr/^{88}Sr = 0{\cdot}1194$. During the analytical period, 100 ppb solutions of standard NBS987 averaged 0·710245 ± 37 (2 SD).

Because a large mass had to be ablated to produce sufficient Sr isotope beam intensities, microphenocrysts were not analyzed by LA-MC-ICPMS. Therefore, to characterize the typical Sr isotope signatures of microphenocrysts and average groundmass in each sample, 0·1 mm diameter microdrill samples were obtained from the matrix from each of the four 100 mm sections in addition to one microphenocryst from the andesitic inclusion. Microdrill samples were analyzed by MC-ICPMS following standard column purification (Ramos, 1992).

RESULTS

Crystal size distribution data

Vesicle-free CSDs using the 3/2 power correction from each of the light dacite, dark andesite, black dacite,

and andesitic inclusion are shown in Fig. 3 and selected CSD data are shown in Table 1. To determine best-fit segmentation for each CSD, linear regressions were performed on different segments within each CSD. For each rock type, the best-fit results (e.g. $R^2 \geq 0{\cdot}93$ for the majority of the data, Table 1) yield three plagioclase size populations that are defined by distinct slopes. These three populations, which are based on crystal length, are: (1) phenocrysts (>0·5 mm); (2) microphenocrysts (0·1–0·5 mm); (3) microlites (<0·1 mm). It is notable that the designations assigned by Clynne (1999) for phenocrysts and microphenocrysts are similar to those defined here. For the four rock types, the absolute values of CSD slopes are greater with decreasing crystal size: 0·9–2·2 for phenocrysts; 12·7–14·9 for microphenocrysts; 26·7–33·5 for microlites (with the exception of inclusion microlites, which have a slope absolute value of 2·6). R^2 values for all of these are ≥0·94, with two exceptions (Table 1).

Because there is some uncertainty about the best method to use in employing a volume correction (as discussed above), we also present CSD data using *CSDCorrections* analyses. Size designations using *CSDCorrections* based on best-fit regression of the CSD segments deviate from the 3/2 method and are as follows: (1) phenocrysts (>1·2 mm); (2) microphenocrysts (0·116–1·2 mm); (3) microlites (<0·116 mm). Absolute values of slopes are: 0·6–1·1 for phenocrysts; 8·2–9·4 for microphenocrysts; 23·2–25·4 for microlites (with the exception of inclusion microlites, which have a slope absolute value of 11·6). R^2 values for these four are ≥0·89 (Table 1). Although, as noted above, *CSDCorrections* results change the size ranges for the crystal populations, each of the four samples can still be divided into three size distinctions with strong R^2 values, similar to those obtained from the 3/2 volume correction. The longer lengths from *CSDCorrections* are not unexpected, as the 3/2 volume correction does not affect the reported length, as it does in *CSDCorrections*. For this study, the 3/2 results are discussed to preserve correlation between the compositional data and crystal lengths that were directly measured from images.

Nomarski textural analysis of Lassen 1915 plagioclase

Microphenocryst textures are typically dominated by well-defined oscillatory zoning (e.g. Anderson, 1983) parallel to crystal edges (Fig. 4a). In some crystals this zoning is truncated by a discontinuity (Fig. 4a–c) that may indicate dissolution of part of the crystal (e.g. Pearce & Kolisnik, 1990). Microlite textures are also dominated by well-defined oscillatory zoning, and in rare cases, dissolution surfaces are evident, but these are less abundant than in the microphenocrysts.

A spectrum of textures exists among Lassen phenocrysts, most of which have been described by Clynne (1999). Unreacted phenocrysts tend to be smooth-textured

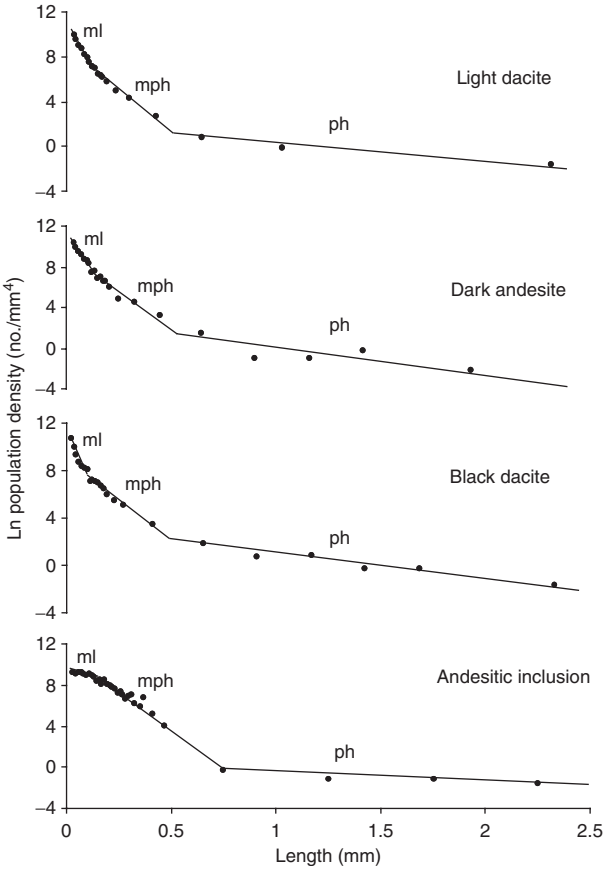

Fig. 3. Plagioclase CSD plots for the four compositions erupted in the 1915 Lassen Peak eruption. Each CSD plot is characterized by three line segments representing three distinct populations of plagioclase: phenocrysts (>0·5 mm), microphenocrysts (0·1–0·5 mm), and microlites (<0·1 mm). Lines represent best-fit linear regressions that define each population. (See Table 1 for selected CSD data.) ml, microlites; mph, microphenocrysts; ph, phenocrysts.

with subdued oscillatory zoning (Fig. 4d). In some cases, more pronounced oscillatory zoning is visible, commonly parallel to crystal edges; truncations of boundaries are mostly absent. Rarely, apparent dissolution surfaces are present, but they tend to have subtle expressions (Fig. 4d). The unreacted portions of reacted crystals have textures similar to unreacted crystals. Reacted portions, which can be concentrated near rims or in cores, or dominate most of the crystals, are cloudy or mottled (Fig. 4e). In most cases, reaction zones are bounded by rounded boundaries. Cloudy regions, which consist of interconnected channels of glass and crystal, are similar to those described by Tsuchiyama & Takahashi (1983). Many reacted crystals have thin (50–100 μm) rims that are characterized by well-defined textural zones that are parallel to crystal edges. A final textural type lacks cloudy zones but shows textural complexity in the form of prominent textural discontinuities (Fig. 4f). In these, faint oscillatory zoning is also present. An additional example of this textural type

Table 1: Crystal size distribution results

Population	No. of crystals	3/2 power correction*			*CSDCorrections**		
		Intercept	Slope	R^2	Intercept	Slope	R^2
Phenocrysts							
LD	20	1·5	−1·4	0·96	1·8	−0·9	0·93
BD (total)	69	2·9	−2·0	0·95	0·5	−1·1	0·98
BD (unreacted)	36†	2·3	−2·1	0·95	—	—	—
INC	18	0·3	−0·9	0·97	3·4	−0·6	0·90
DA	34	2·0	−2·2	0·62	−0·4	−1·5	0·95
Microphenocrysts							
LD	139	8·7	−14·9	0·98	7·8	−9·4	0·98
BD	133	8·8	−14·1	0·98	7·5	−8·4	0·90
INC	621	10·5	−12·7	0·94	9·6	−8·2	0·99
DA	147	9·1	−14·2	0·95	7·6	−8·2	0·96
Microlites							
LD	1666	11·0	−32·3	0·99	11·8	−25·4	0·98
BD	992	10·9	−33·5	0·94	11·4	−25·0	0·97
INC	1100	9·3	−2·6	0·33	10·3	−11·6	0·89
DA	1678	11·1	−26·7	0·99	11·8	−23·2	0·99

LD, light dacite; BD, black dacite; INC, andesitic inclusion; DA, dark andesite.
*Details of volume correction provided in text.
†A separate calculation was performed for only unreacted phenocrysts to test the viability of calculating CSDs from reacted phenocrysts (andesitic inclusion) and reacted + unreacted phenocrysts (light and black dacite, and dark andesite).

is found in a phenocryst from an inclusion that has a measured long dimension of 0·58 mm, which is close to the lower size limit for phenocrysts (Fig. 4g).

Plagioclase and glass major element analyses

Table 2 presents selected major element data for plagioclase from the 1915 eruption; the full dataset is available in Electronic Appendices 1 and 2 on the Journal of Petrology website at http://www.petrology.oxfordjournals.org. Figure 5a summarizes the relationship between An content of phenocrysts, microphenocrysts and microlite cores and crystal sizes measured directly by NIH Image. There is a clear correlation between crystal size (length) and An core content. With the exception of rare xenocrystic plagioclase and two andesitic inclusion phenocrysts, the phenocryst core analyses range from An_{29} to An_{42}, and the averages $\pm 1\sigma$ for light dacite, black dacite, and dark andesite are $33{\cdot}9 \pm 6{\cdot}3$, $36{\cdot}0 \pm 4{\cdot}8$, $36{\cdot}1 \pm 5{\cdot}6$, respectively (Table 3). This An range is consistent with the more extensive database reported for these units by Clynne (1999). The two analyzed inclusion phenocrysts that are transitional in size (520 and 580 μm) between microphenocrysts and phenocrysts have average ($\pm 1\sigma$) An of 62·4 (±9·8). These two crystals probably belong to the microphenocryst population. Microphenocrysts have core An values between An_{59} and An_{82}, with averages ($\pm 1\sigma$) from $66{\cdot}1 \pm 4{\cdot}1$ to $69{\cdot}5 \pm 4{\cdot}5$ (Table 3). Microlites are characterized by $An_{40–67}$ and, with the exception of the 'transitional' inclusion phenocrysts noted above, are the only crystal population in which a correlation between rock type and anorthite content exists. Microlites from the dark andesite are more anorthitic ($An_{60–66}$) than those from the other three rock types ($An_{40–59}$). This distinction is revealed by examining averages ($\pm 1\sigma$) for light dacite, black dacite and inclusion: these values are 53·1 (±7·1), 56·7 (±7·7), and 51·7 (±5·7), respectively, whereas the dark andesite values are 63·5 (± 2·0).

Unlike plagioclase cores, the compositions of plagioclase rims are not correlated with crystal length (Fig. 5b). Phenocryst ($An_{32–72}$), microphenocryst ($An_{40–67}$), and microlite ($An_{41–64}$) rims show significant variations within each size range, and, in contrast to core data, there is a great degree of overlap between composition and size. However, some correlations exist among composition, size, and rock type. Microphenocryst rims in the dark andesite are more anorthitic ($An_{57–66}$) than those in the other three rock types ($An_{40–58}$), which are generally similar (see Table 3 for comparison of averages and standard deviations). Similarly, microlite rims in the dark andesite are also more anorthitic ($An_{60–64}$) than the other microlites ($An_{41–53}$). Among the three crystal size populations, most crystals show extensive zoning. Comparison of average core and rim values for the four compositional products show that all microlite populations are normally zoned (Table 3). Zoning is mostly normal for the microphenocryst population, and the dark andesite again has the most An-rich rims. In all cases, average rim compositions of the two populations are within several An mol % for each product. For example, inclusion averages for microlites and microphenocrysts are An 44·8 and 46·4, respectively. Overgrowths on reacted phenocryst rims are reversely zoned, whereas unreacted rims show minor normal zoning.

Glass major element microprobe analyses normalized on an anhydrous basis for the four compositional types are summarized in Table 4, including average analyses with standard deviations. In general, matrix glass from the light dacite, black dacite, and the andesitic inclusion are similar in composition. They have ~71–75 average wt % SiO_2 and 3·2–4·2 average wt % K_2O. Consistent with the higher An contents of the dark andesite microlite cores and rims, the dark andesite is characterized by distinctly more mafic (~65 wt % average SiO_2 and 2·4 wt % average K_2O) glass. Some heterogeneity in the matrix glass composition is evident as illustrated by the higher standard deviations for SiO_2, particularly in the black dacite and

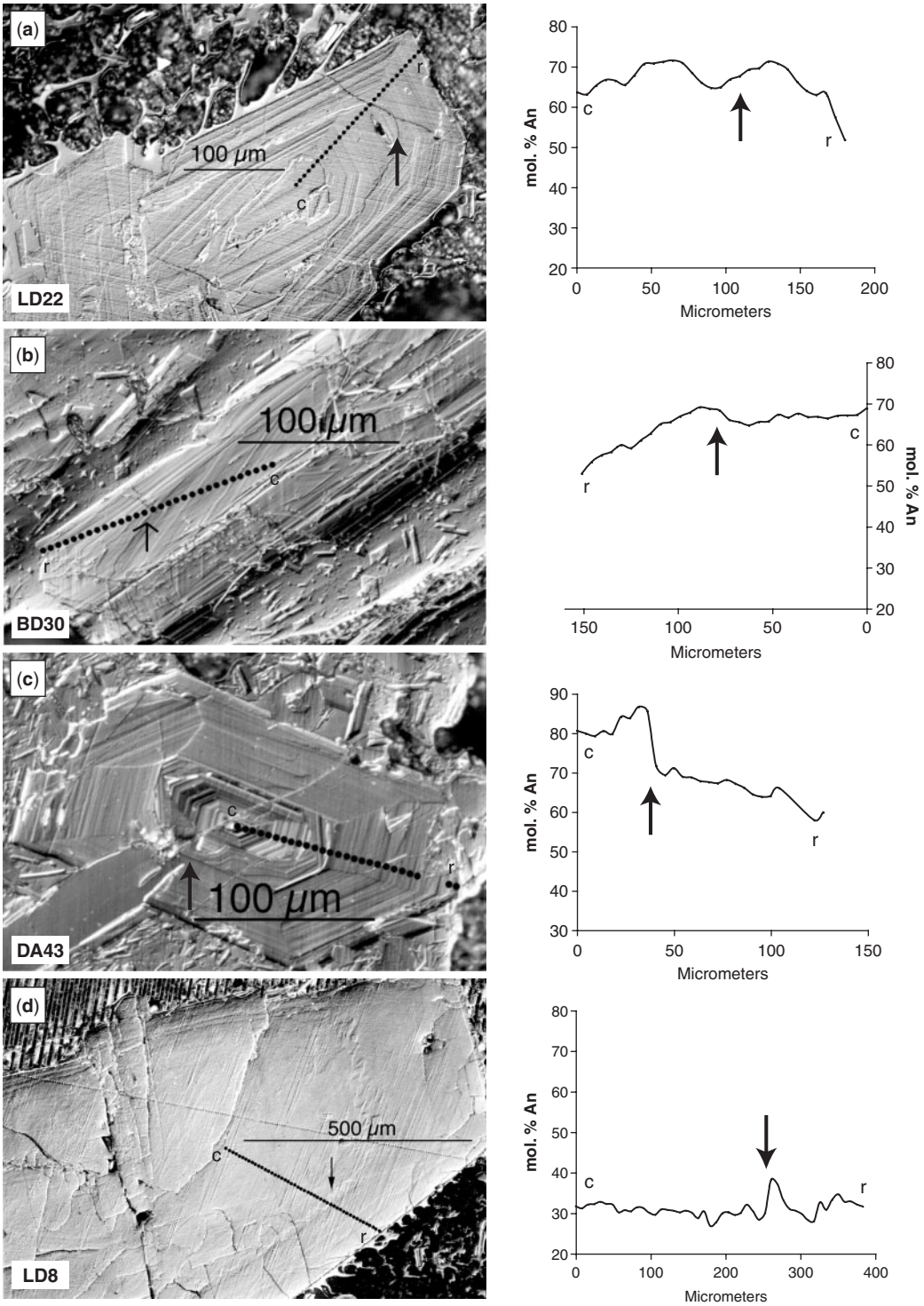

Fig. 4. Nomarski differential interference contrast images paired with electron microprobe data (An mol% vs core-to-rim location of microprobe traverse) for selected microphenocrysts (a–c) and phenocrysts (d–g). Arrows show the location of prominent textural discontinuities. (e) and (f) show locations of troughs generated by laser *in situ* analyses for Sr isotopes. Trough number corresponds to analysis number in Table 7. c, approximate core of crystal; r, rim of crystal.

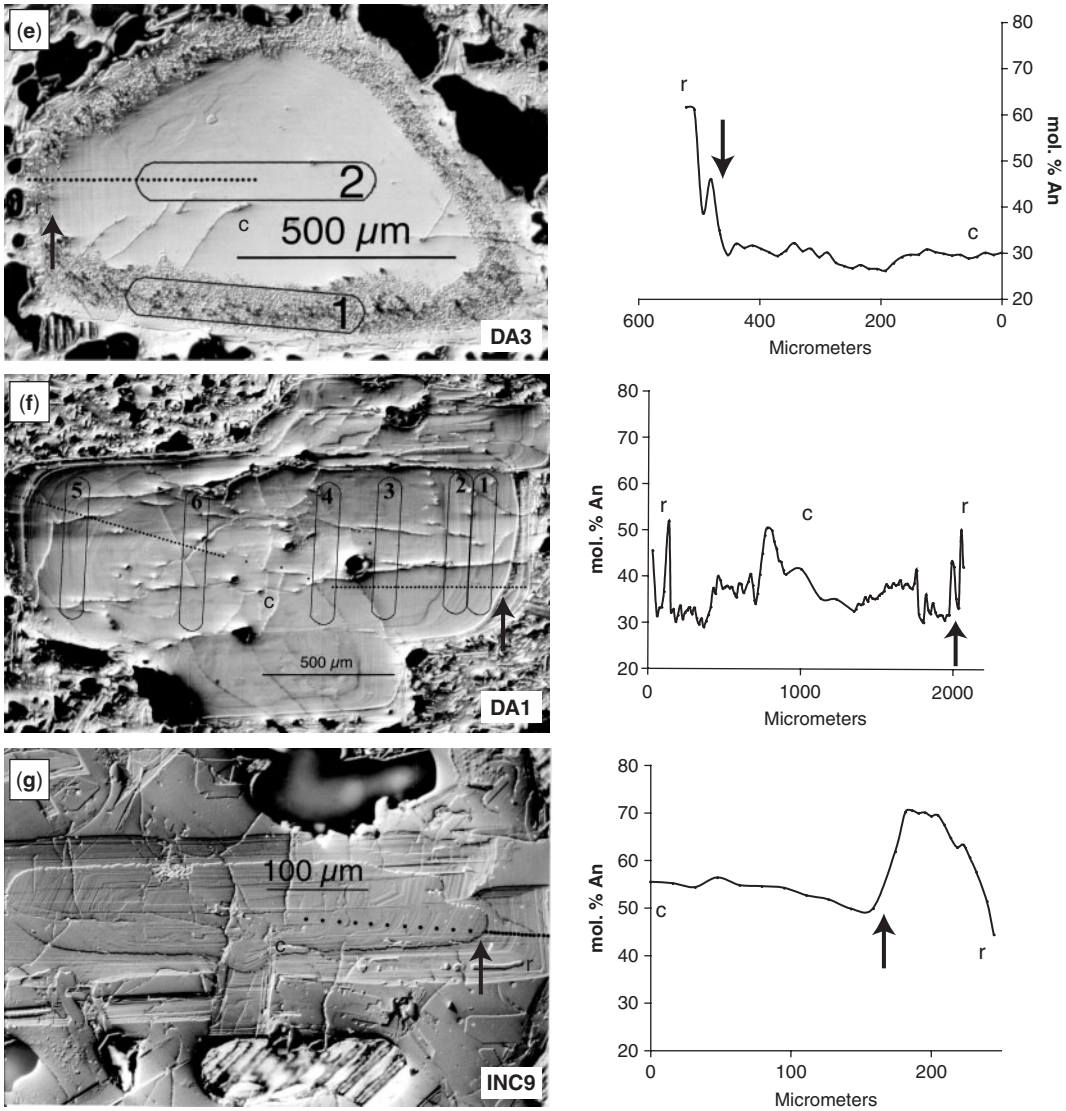

Fig. 4. Continued

dark andesite. This heterogeneity may reflect analysis of small crystals not resolvable during electron microprobe analysis or local effects of microlite crystallization.

Plagioclase major element traverses combined with NDIC textural data

Electron microprobe traverses of selected plagioclase microphenocrysts ($n = 9$) and phenocrysts ($n = 4$) that display the range of textures described above, and as revealed by NDIC imaging, were conducted to provide compositional context for textural variations. Table 5 provides a summary of characteristics for all traverses, and selected results are summarized in Fig. 4. A typical traverse involved an analysis every 5–10 μm from near the core to the rim. In one case (DA1), a rim-to-rim traverse of a phenocryst was completed. A complete set of NDIC images has been given by Salisbury (2003) and microprobe traverse data are available in Electronic Appendix 3.

Microphenocryst traverses are dominated by gradual (<4 mol % An per 10 μm) major element compositional changes, and Table 5 shows that all analyzed microphenocrysts are broadly normally zoned. For example, in BD30 (Fig. 4b), anorthite content varies from ~An_{70} to An_{53} over a distance of ~150 μm from core to rim; the average An decrease for each step (~5 μm) is 0·6. In DA12, An decreases from 68 to 59, with an average 0·3 decrease per step (~8 μm). Three of the nine microphenocrysts traversed (i.e. LD4, LD22, DA43) have rims characterized by slightly larger An variations, up to 12 mol % over the last few micrometers (see Table 5 for details). A number of microphenocrysts show textural discontinuities (e.g. LD22, BD30, LD4) (Fig. 4a and b), but across these zones, An

Table 2: Selected major element microprobe data for plagioclase cores and rims of four rock types from the 1915 Lassen Peak eruption

Sample label	Size (μm)	SiO_2	Al_2O_3	CaO	Na_2O	K_2O	FeO*	MgO	Total	An (mol%)	Ab (mol%)	Or (mol%)
Core data												
LD34a c	45	53·73	27·95	10·87	4·92	0·26	0·67	0·07	98·47	54·1	44·3	1·5
LD3 c	220	52·22	30·07	13·17	3·95	0·15	0·57	0·16	100·3	64·3	34·9	0·9
LD8 c	1349	61·34	24·52	6·01	7·59	0·59	0·21	0·02	100·3	29·4	67·2	3·4
DA41 c	83	52·83	29·54	12·83	4·06	0·16	0·82	0·18	100·4	63·0	36·1	1·0
DA6 c	351	51·63	31·12	14·13	3·44	0·10	0·60	0·15	101·2	69·0	30·4	0·6
DA3 c	550	60·18	24·26	6·52	7·23	0·59	0·15	0·02	98·95	32·1	64·4	3·4
BD3b c	46	53·10	28·34	11·61	4·59	0·24	0·84	0·10	98·82	57·5	41·1	1·4
BD33 c	200	50·02	31·28	14·70	3·26	0·15	0·68	0·10	100·2	70·7	28·4	0·8
BD22 c	729	58·28	25·45	7·59	7·09	0·53	0·25	0·02	99·21	36·1	61·0	3·0
INC34a c	59	56·41	27·52	10·18	5·46	0·29	0·43	0·03	100·3	49·9	48·4	1·7
INC21 c	250	51·08	30·69	14·11	3·48	0·14	0·56	0·14	100·2	68·6	30·6	0·8
INC8 c	520	50·30	31·32	14·14	3·37	0·14	0·27	b.d.	99·54	69·3	29·9	0·8
INC9.1__1	580	53·32	28·34	11·37	4·92	0·20	0·35	0·04	98·54	55·4	43·4	1·2
Rim data												
LD34d r	91	56·96	25·78	9·20	5·43	0·62	0·73	0·09	98·81	46·6	49·7	3·7
LD4 r	271	54·78	27·98	10·77	5·16	0·27	0·67	0·08	99·71	52·7	45·7	1·6
LD16 r	440	56·60	27·35	10·38	5·22	0·35	0·63	0·04	100·6	51·3	46·7	2·1
LD11 r (og)	2384	51·22	31·22	14·14	3·42	0·12	0·54	0·13	100·8	69·1	30·2	0·7
BD34 r	60	55·18	26·88	9·89	5·53	0·37	0·67	0·09	100·7	48·7	49·6	1·7
BD30 r	377	56·93	25·99	9·19	5·68	0·53	0·68	0·05	100·6	43·6	54·4	1·9
BD22 r	729	52·75	29·03	12·20	4·63	0·19	0·65	0·11	100·1	56·3	42·5	1·2
BD1 r (og)	951	50·12	31·45	14·76	3·12	0·13	0·64	0·11	97·49	44·4	53·2	2·4
BD10 r	1121	55·94	26·25	9·05	5·87	0·44	0·42	0·05	99·21	63·0	36·2	0·8
BD11 r	1396	60·39	25·09	6·99	7·32	0·57	0·28	b.d	98·69	61·4	37·5	1·1
INC32a r	46	56·39	27·68	10·09	5·67	0·30	0·52	0·04	99·74	61·6	37·3	1·1
INC22 r	128	57·93	26·80	8·94	6·17	0·33	0·39	0·02	98·87	61·6	37·4	1·0
INC8 r (og)	520	54·38	28·54	11·54	4·81	0·20	0·55	0·04	100·0	31·6	65·2	3·2
INC9__2	580	56·11	25·44	8·92	5·91	0·41	0·65	0·05	98·61	48·6	49·2	2·2
INC3 r (og)	798	51·93	29·51	12·79	4·05	0·14	0·69	0·10	99·05	45·7	51·1	3·1
DA48b r	36	52·24	28·69	12·33	4·16	0·18	0·90	0·19	99·56	58·7	40·2	1·1
DA12 r	307	52·71	28·87	12·63	4·22	0·18	0·94	0·19	100·3	71·8	27·4	0·7
DA3.39 (og)	550	51·98	29·27	12·49	4·19	0·17	0·68	0·09	98·02	44·8	52·6	2·6
DA1 r	2006	60·91	24·59	6·45	7·35	0·55	0·18	0·01	100·6	33·4	63·3	3·3

Sample abbreviations as in Table 1; c, core; r, rim; og, overgrowth; b.d., below detection. Size (μm) refers to long axis and is result of CSD measurement. Major elements in wt%.
*All iron calculated as FeO.

contents change only slightly (up to 4 mol %) over distances of ~5–10 μm. Major intracrystal An variations are rare. DA43 in the dark andesite is the only traversed microphenocryst that has a major decrease in An content (14 mol %) in the interior of the crystal (between 30 and 41 μm from core); interestingly, the textural discontinuity associated with this change is not necessarily the most prominent one (Fig. 4c). Following this change, DA43 records small changes in An (0–3 mol % over 5 μm intervals) to near the rim, which varies from An_{66} to An_{58} a few micrometers from the rim.

Almost all unreacted phenocrysts analyzed with the Nomarski technique revealed very little textural variation, so those showing the most prominent dissolution surfaces

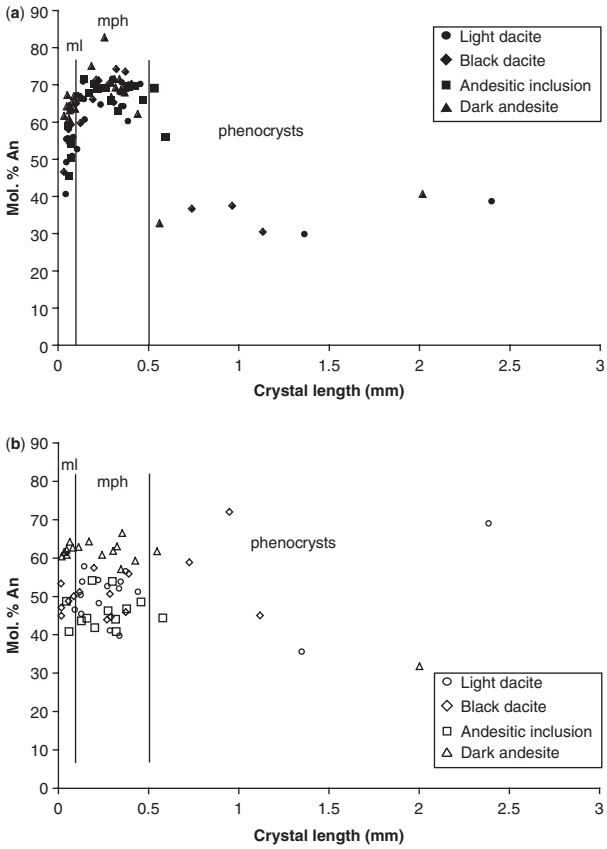

Fig. 5. (a) Core An content (mol %) vs crystal length measured in NIH Image from X-ray images. Vertical lines represent divisions between three crystal populations. (b) Rim An content (mol %) vs crystal length measured in NIH Image from X-ray images.

Table 3: Average An data for cores and rims of plagioclase crystal size populations

	Microlite core	Microphenocryst core	Phenocryst core	Microlite rim	Microphenocryst rim	Phenocryst rim
All types						
Average	57·3	68·0	35·5*	53·6	51·7	51·8
SD	29·0	4·1	4·6	7·9	7·2	14·5
n	27	47	8	14	38	11
Light dacite						
Average	53·1	66·1	33·9	one crystal	50·6	52·4
SD	7·1	4·1	6·3	—	5·6	23·7
n	9	11	2	1	13	2
Black dacite						
Average	56·7	68·4	36·0	48·7	49·8	52·2
SD	7·7	4·2	4·8	3·2	5·4	16·7
n	4	11	4	5	7	4
Andesitic inclusion						
Average	51·7	67·6	62·4*	44·8	46·4	54·6
SD	5·7	2·5	9·8	5·6	4·6	9·4
n	4	10	2	2	10	3
Dark andesite						
Average	63·5	69·5	36·1	61·8	61·8	46·6
SD	2·0	4·5	5·6	1·4	2·9	21·2
n	10	15	2	6	8	2

Sample abbreviations as in Table 1; *n*, number of crystals in population. SD, standard deviation.
*Two inclusion phenocrysts excluded from calculation of average An core value for all phenocrysts.

were chosen for detailed microprobe traverses. In general, as for microphenocrysts, changes in An content are not significant over 5–10 μm intervals. The An contents of the cores are nearly constant as shown by the traverse of LD8 (Fig. 4d). An increase of only 8 mol % An (from An_{30} to An_{38}) corresponds to a subtle textural discontinuity located ~250 μm from the first core analysis.

Phenocrysts with mottled zones characteristically show large variations in An (e.g. crystal DA3, Fig. 4e). The interior portion of this crystal shows little variation, remaining near An_{30} until the mottled zone at the exterior, where composition fluctuates from ~An_{35} to An_{60} over the last ~70 μm.

Crystal DA1 in the dark andesite does not show mottled reaction textures, but does show several prominent textural discontinuities. This crystal was analyzed for major elements from rim to rim across the long axis of the crystal (Fig. 4f); from core to rim, An varies from An_{29} to An_{52}. Most of the crystal is characterized by small (<3 mol %) changes, but the outer 100 μm contains large anorthite perturbations. For example, over this distance, the An content of the left rim of the crystal (as shown in Fig. 4f) varies from 45 down to 31, up to 51 and down to 32. Similar changes are observed on the right rim. These An variations are associated with prominent textural discontinuities. Similarly, several other major textural zones are associated with relatively large changes in An over tens of micrometers, but crystals like DA1 are rare, and the maximum An recorded in this crystal is 52. INC9 also displays at least one prominent textural discontinuity (between 159 and 182 μm from the core) in the absence of a mottled zone. This discontinuity is correlated with a large (20 mol %) change in An (Fig. 4g). Following a rimward increase from ~An_{50} to An_{70}, An decreases to An_{44}, including an abrupt change from An_{58} to An_{44} over the last 13 μm.

Plagioclase trace element data

Laser ablation ICP-MS data for Sc, Rb, Sr, Y, Ba, La, Ce, Nd, Sm, Eu, and Pb are reported in Table 6. Analysis location (i.e. location of the laser pit) is tied to the electron microprobe traverse shown in Fig. 4. Analysis coordinates

Table 4: Glass major element microprobe data normalized to 100%

Sample	SiO_2	Al_2O_3	CaO	MgO	FeO*	Na_2O	K_2O	Total[1]
Light dacite								
LD4.2__9	73·51	14·84	2·45	0·28	1·72	3·68	3·52	96·58
LD4.2__10	75·80	13·22	1·45	0·34	1·77	3·46	3·97	96·76
LD12·1__11	75·33	13·75	1·69	0·36	1·97	2·97	3·92	96·23
LD12.1__12	75·43	13·20	1·53	0·36	2·17	3·33	3·98	95·22
LD8.1__50	74·84	13·37	1·64	0·35	2·11	3·71	3·99	96·85
Average	74·98	13·68	1·75	0·34	1·95	3·43	3·87	96·30
SD	0·89	0·69	0·40	0·03	0·20	0·30	0·20	0·66
Black dacite								
BD3 glass2	76·95	12·44	0·87	0·22	1·80	3·14	4·58	98·88
BD1 glass	77·49	11·50	0·72	0·53	2·21	2·92	4·63	98·58
BD3a.2__9	65·58	20·30	5·42	0·07	1·16	5·54	1·93	98·09
BD27__13	63·41	22·04	6·76	0·25	1·02	4·99	1·53	98·34
Average	70·86	16·57	3·44	0·27	1·55	4·15	3·16	98·46
SD	7·40	5·37	3·11	0·19	0·56	1·31	1·67	0·33
Andesitic inclusion								
INC glass3	74·99	14·39	1·14	0·30	2·35	2·62	4·21	97·02
INC glass2	75·15	14·30	1·08	0·27	1·92	3·01	4·27	98·40
INC glass1	73·85	14·37	1·36	0·40	2·65	3·03	4·33	99·02
INC glass1	71·86	14·39	1·44	0·57	3·00	4·46	4·27	96·99
INC12.2__19	76·01	13·31	1·08	0·22	2·00	3·41	3·97	96·47
INC12.2__20	75·74	13·57	1·01	0·24	2·02	3·21	4·21	96·56
Average	74·60	14·05	1·19	0·33	2·32	3·29	4·21	97·41
SD	1·54	0·49	0·17	0·13	0·43	0·63	0·13	1·05
Dark andesite								
DA glass1	70·10	14·54	2·98	0·70	4·51	3·85	3·32	98·94
DA glass2	66·87	12·78	4·27	3·29	6·50	3·26	3·03	97·94
DA glass3	62·21	10·45	5·26	6·88	10·38	2·79	2·02	99·11
DA12.2__19	62·02	18·41	6·73	2·17	4·73	4·06	1·87	97·21
DA12.2__20	65·44	13·96	4·17	2·58	7·46	3·70	2·69	95·95
DA21.2__29	63·97	15·42	5·03	3·25	6·32	3·90	2·11	96·97
DA6.1__22	63·20	17·73	6·31	2·04	4·67	3·92	2·13	96·66
Average	64·61	14·68	5·00	3·23	6·53	3·59	2·37	97·54
SD	2·76	2·57	1·20	1·91	1·99	0·45	0·57	1·18

Abbreviations as in Tables 1 and 2.
*All iron calculated as FeO.
[1]Pre-normalized totals.

are measured in micrometers and start at or near the core (i.e. a coordinate of 0 represents the start of the electron microprobe traverse). Coordinate mid-point represents the average position of the laser pit. Figures 6 and 7 show An or size vs selected trace element concentration. Analyzed crystals include two microphenocrysts (LD22, INC12), and four phenocrysts (DA3, DA1, LD8, INC9), although of these four, two have crystal sizes near the microphenocryst–phenocryst boundary (DA3 and INC9).

An contents of these crystals range from ~70 to 28. The two microphenocrysts have relatively uniform An contents between 65 and 70 whereas three of the four phenocrysts have An between ~28 and 41. One phenocryst (INC9, ~0·58 mm) has An between 51 and 70. Comparison of An contents vs trace element concentration reveals three broad types of trends, regardless of analysis location (Fig. 6 and Table 6). An vs Pb, Ba, La, Ce, Rb and Sc form negatively correlated trends. The An vs Pb, Ba, La and Ce trends show a relatively narrow range of concentrations for the

Table 5: Summary characteristics of microprobe traverses and textural data for plagioclase microphenocrysts and phenocrysts

Sample	Crystal size (μm)	Core An (mol%)	Rim An (mol%)	Average step size (μm)	Average ΔAn*	Comments
DA43	246	81	60	5·1	−0·8	At 30–41 μm from core, large change in An from 86 to 72; at 104–122 μm from core (near rim) An change from 66 to 58; textural complexity observed, but most extreme feature not correlated with large An changes
LD4	271	68	53	6·9	−1	Last 10 μm, change from An_{64} to An_{58}; major textural discontinuities observed but not correlated with large An change
DA12	307	68	59	7·8	−0·3	Crystal dominated by edge-parallel textural zones
INC12	318	68	56	5·8	−0·5	Some subtle textural discontinuity observed, but no An changes ≥3 mol% An per step noted
DA21	328	69	62	4·9	−0·2	Some textural discontinuity observed, but no An changes ≥3 mol% An per step
LD22	336	64	52	6·4	−0·4	Last 12 μm, change from An_{64} to An_{52}; textural discontinuity observed, but no An changes ≥3 mol% An per step
DA6	351	68	58	4·9	−0·5	Some subtle textural discontinuity observed, but no An changes ≥3 mol% An per step
BD13	361	72	63	9·1	−0·6	Some subtle textural complexity, but no An changes ≥3 mol% An per step
BD30	394	69	53	5·2	−0·6	Subtle textural discontinuity observed, but no An changes ≥3 mol% An per step
DA3	550	30	62	13·7	0·8	Crystal zoned from An_{30} to An_{46} at 0–480 μm from core; near rim, zoned from An_{39} to An_{62} (at 494–521 μm from core) in mottled/dusty region
INC9	580	55	44	9·8	−0·4	An change from 50 to 70 at 159–183 μm from core, associated with prominent textural discontinuity; An change from 58 to 44 near rim (232–245 μm from core)
LD8	1349	32	32	8·1	0·0	All steps ≤4 mol% (normally zoned) except at 253–261 μm from core, An change from 30 to 38, where a subtle textural discontinuity is observed
DA1	2006	45	42	19·6†	−0·03	Most of crystal dominated by small An changes (≤3 mol %); several regions marked by abrupt changes in An over small distances; some An changes associated with textural discontinuities

Abbreviations as in Table 1.
*Represents average change in An content from step x to step $x+1$, starting from core. Unless otherwise noted in comments, ΔAn for each step is ≤4 mol%.
†Average includes large steps near core of crystal. Otherwise, average step size is 15·9 μm.

microphenocrysts and the rim of INC9, transitional values for the intermediate and core areas of INC9, and higher values for the remaining phenocrysts (Fig. 6a). Rb and Sc form broad negative trends that are more diffuse. Y, Nd, Sm, and Eu exhibit a second type of trend. At higher An, these elements are negatively correlated, but with only a few exceptions, at lower An, element abundances are similar to or lower than values for the $An_{50–60}$ range (INC9) (Fig. 6b). A third type of trend characterizes Sr. Higher An crystals have a range of Sr concentrations from ~1200 to 700 ppm. INC9, which has intermediate An values, ranges in Sr from ~1380 to 1050 ppm, and the remaining phenocrysts with An <41·5 are characterized by Sr concentrations between 1070 and 700 ppm. There are no clear correlations between crystal size and Sc, Rb, Sr (Fig. 7c), and Y, again regardless of analysis location within

Table 6: Laser ablation ICP-MS trace element data for plagioclase

Sample no.	Crystal length (μm)	An (mol %)	Analysis location	Analysis coordinates*	Coordinate mid-point†	CaO (wt %)‡	Sc§	Rb	Sr	Y	Ba	La	Ce	Nd	Sm	Eu	Pb
INC12-C1	318	68·2	core	0–27	13·5	13·89	1·41	0·34	1186	0·16	108	1·52	2·38	0·75	0·11	0·34	1·07
INC12-C2	318	66·6	inter	41–82	61·5	14·07	1·49	0·30	1175	0·14	101	1·77	2·67	0·92	0·10	0·39	1·24
INC12-R1	318	65·2	rim	109–143	126	10·82	1·11	0·15	860	0·10	68	1·18	1·87	0·60	0·07	0·28	0·89
LD22-C-1	336	64·0	core	0–6	3	12·86	1·51	0·71	1032	0·22	83	1·54	2·50	0·83	0·10	0·29	1·19
LD22-R-1	336	64·2	mid	140–172	156	10·40	1·58	0·17	830	0·15	76	1·37	2·06	0·65	0·11	0·26	0·96
LD22-C-2	336	70·1	near rim	45–83	64	13·18	1·34	0·16	1039	0·12	81	1·23	1·95	0·59	0·08	0·27	0·88
DA3-C-1	550	30·0	core	0–14	7	6·13	2·29	1·23	816	0·28	668	11·1	12·5	2·10	0·29	1·04	10·93
DA3-R-1	550	30·9	rim	343–439	391	6·26	2·05	0·78	797	0·23	506	9·92	11·8	1·99	0·27	1·00	9·92
DA3-R-2	550	36·4	rim	439–494	466·5	6·26	2·00	0·69	781	0·18	503	10·2	11·9	2·01	0·20	0·98	9·22
DA3-C-2	550	27·8	inter	151–219	185	5·43	1·83	0·84	712	0·16	509	9·02	10·2	1·75	0·14	0·87	8·37
INC9-C1	580	55·0	core	0–16	8	11·37	1·47	0·49	1165	0·25	152	3·93	5·94	1·52	0·21	0·64	3·06
INC9-C2	580	54·0	inter	79–111	95	10·00	1·27	0·25	1044	0·24	144	4·71	7·15	2·06	0·24	0·68	3·30
INC9-C3	580	50·7	inter	127–159	143	13·88	1·93	0·34	1377	0·30	258	6·88	9·98	2·44	0·28	0·96	4·92
INC9-C4	580	69·4	near rim	182–209	195·5	8·92	0·94	0·12	701	0·10	56	0·87	1·36	0·46	0·09	0·22	0·62
LD8-C-1	1349	31·8	core	0–24	12	6·41	2·03	7·50	787	0·42	534	11·2	13·4	2·34	0·26	0·92	10·96
LD8-R-1	1349	32·3	rim	318–375	346·5	5·77	1·49	0·69	735	0·15	441	9·27	10·6	1·81	0·16	0·86	8·79
LD8-C-2	1349	31·3	inter	212–261	236·5	6·06	1·49	0·66	763	0·15	473	9·94	11·5	1·96	0·16	0·87	8·58
LD8-C-3	1349	30·6	inter	65–114	89·5	6·12	1·66	0·71	775	0·15	512	10·0	11·3	2·01	0·14	0·94	9·30
LD8-C-4	1349	29·4	inter	139–187	163	5·91	1·58	0·68	758	0·15	490	9·31	10·6	1·87	0·15	0·91	8·88
DA1-C-1	2006	41·3	core	874–904	889	9·20	2·29	1·08	1072	0·26	396	8·06	11·0	2·45	0·28	0·98	9·35
DA1-C-2	2006	37·1	inter	491–598	544·5	7·65	1·78	0·43	953	0·17	327	8·12	9·89	1·86	0·16	0·80	8·17
DA1-R-1	2006	32·1	near rim	184–291	237·5	8·61	2·50	0·91	1067	0·22	652	13·9	15·8	2·85	0·21	1·26	12·02
DA1-C-3	2006	37·6	inter	613–736	674·5	6·85	1·48	0·37	806	0·21	282	6·78	9·06	2·05	0·20	0·69	5·92
DA1-C-4	2006	34·9	inter	1381–1473	1427	7·07	1·71	0·48	895	0·17	333	8·23	10·3	1·94	0·17	0·78	7·47
DA1-C-5	2006	38·3	inter	1610–1717	1663·5	7·55	1·74	0·43	954	0·15	331	8·53	10·4	1·93	0·17	0·79	7·50
DA1-C-6	2006	35·0	core	1132–1236	1184	5·90	1·39	0·79	727	0·29	316	4·82	6·63	1·92	0·21	0·69	5·27
DA1-R-2	2006	34·0	near rim	1931–1992	1961·5	8·61	1·61	0·95	843	0·54	301	6·91	9·07	2·08	0·30	0·77	7·68

Abbreviations as in Table 1.
*Beginning and ending coordinates of laser ablation spot (in μm). Coordinate measurements referenced to microprobe traverse.
†Average coordinate position is mid-point of laser ablation spot.
‡CaO (wt %) from electron microprobe analysis was used as an internal standard for data reduction.
§Trace elements in ppm.

a crystal. Phenocryst and microphenocryst ranges overlap. In contrast, microphenocrysts have relatively low Ba, La, Ce, Nd, Sm, Eu, and Pb concentrations compared with most phenocrysts (Fig. 7a and b). It should be noted that for INC9, which is transitional in size, concentrations approach or overlap those of phenocrysts. The exception is the high An rim value of INC9, which typically has elemental abundances similar to those of microphenocrysts. This observation reinforces the correlation observed between concentrations of these elements and An contents.

Finally, because trace element analyses were obtained by laser ablation, relationships between element concentrations and positions in crystals (i.e. core vs intermediate vs rim) were evaluated. The position of each analysis within the crystal was estimated using the average of the start and end points of each laser pit along the electron microprobe traverse (Fig. 4 and Table 6). Overall, there are no simple correlations between positions and trace element concentrations. However, several detailed observations are relevant to the correlations noted above: (1) with the exception of Sr, trace element concentrations of the near-rim spot of phenocryst INC9 are similar to those of the microphenocrysts. Because this spot has $\sim An_{70}$ (similar to An contents of the microphenocrysts), this again reinforces the correlation between element concentration and An content. (2) Of all the crystals analyzed,

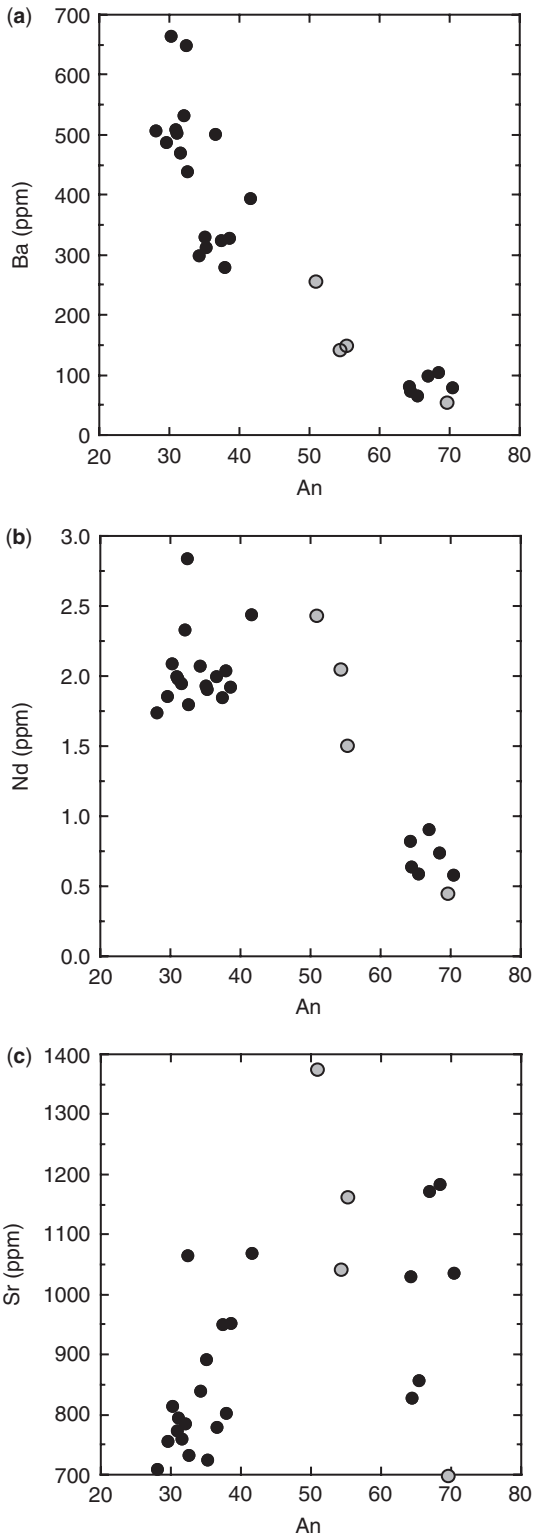

Fig. 6. Trace element concentrations vs An content (mol %) of plagioclase. Gray-filled circles represent analyses of INC9. (See text for discussion.)

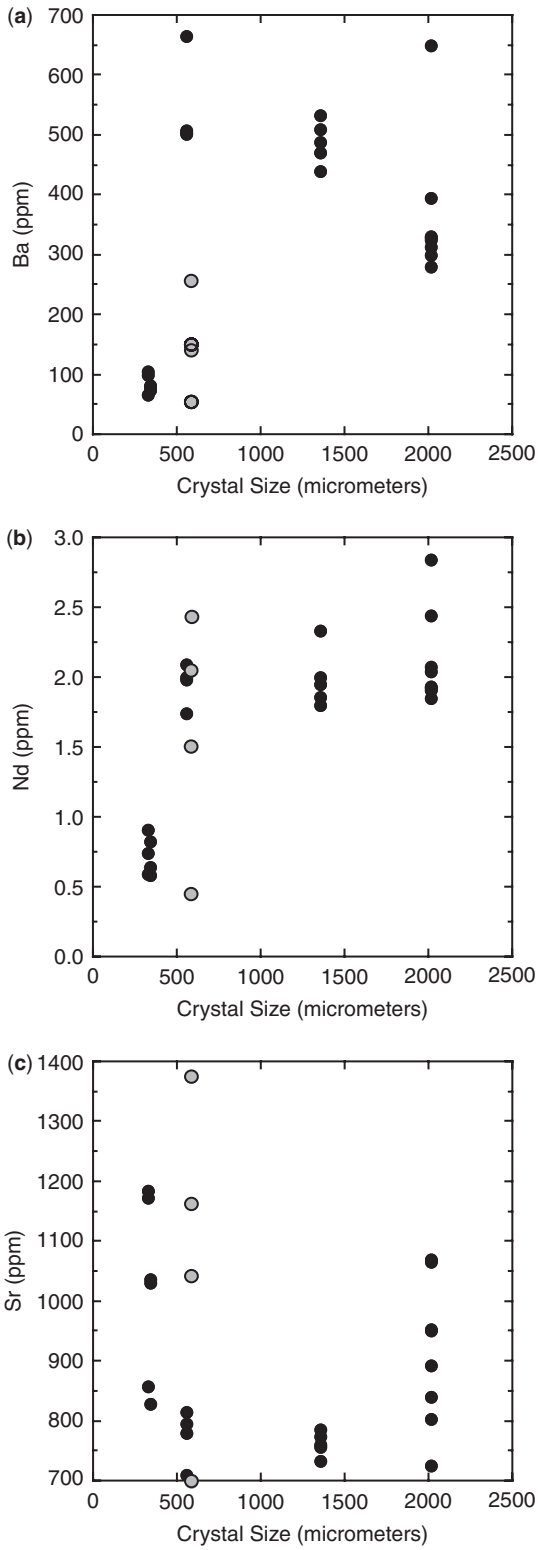

Fig. 7. Trace element concentrations vs plagioclase crystal size. Gray-filled circles represent analyses of INC9. (See text for discussion.)

LD8, which has small core-to-rim variations in An (Fig. 4d), shows smooth zoning from core to rim in Ba and Sr; both decrease from core to rim. La, Ce, Nd, and Pb also decrease from core to rim, but there is more variation in the intermediate points. Sm, Y, and Eu do not show simple trends. Of the phenocrysts analyzed for trace elements, LD8 has the simplest texture, exhibiting only one subtle textural discontinuity that is associated with a small An increase.

Sr isotope data

In situ laser ablation Sr isotope data for a small number of phenocrysts from each of the four compositions are presented in Table 7. In all cases, multiple analyses (i.e. troughs) were acquired for each crystal. Figures 4 (crystals for which there are microprobe and trace element data) and 8 (crystals for which there are no microprobe data) show NDIC images of each analyzed crystal, together with approximate locations of each laser ablation trough. Figure 9 summarizes the relative locations of each trough vs Sr isotope ratio. $^{87}Sr/^{86}Sr$ ranges from ~0·7040 to 0·7045, with an average 2σ uncertainty of ±0·000053. Of the seven phenocrysts analyzed, five display intracrystal variations outside analytical error (LD12, LD1, DA1, BD11, DA20), whereas multiple analyses of BD7 and DA3 show no resolvable intracrystal variations. Although $^{87}Sr/^{86}Sr$ varies among and within phenocrysts, systematic core-to-rim variations are not observed, despite textural differences (reacted vs unreacted zones). Similarly, no discernible patterns are observed between Sr isotope signatures and compositions. We recognize, however, that our interpretations are limited by the small dataset, the location of the ablation troughs, and the resolution of the laser.

The small sizes and low Sr contents of some crystals precluded analysis by laser, so one crystal from the inclusion (INC43; measured NIH Image length 204 μm) was drilled. The core of a crystal in sample INC43 has $^{87}Sr/^{86}Sr$ of ~0·7041. This crystal has a texture typical of microphenocrysts in all samples. $^{87}Sr/^{86}Sr$ values from microdrill analyses of groundmass from each of the four rock types are remarkably homogeneous, with an average value of 0·704261 ±55. Uncertainty of $^{87}Sr/^{86}Sr$ for the light dacite sample is fairly large because the high vesicularity of the groundmass limited the mass of sample recovered during drilling.

Table 7: $^{87}Sr/^{86}Sr$ (±2σ) laser or microdrill data

Sample	$^{87}Sr/^{86}Sr$
LD12-1	0·704316 ± 42
LD12-2	0·704241 ± 42
LD12-3	0·704293 ± 80
LD12-7	0·704441 ± 47
LD12-4	0·704317 ± 50
LD12-8	0·704533 ± 47
LD12-5	0·704498 ± 78
LD1-1	0·704505 ± 56
LD1-2	0·704318 ± 44
LD1-3	0·704337 ± 30
LD1-4	0·704485 ± 52
LD1-5	0·704369 ± 50
BD7-1	0·704364 ± 30
BD7-2	0·704370 ± 45
BD7-3	0·704382 ± 59
BD7-4	0·704403 ± 53
BD11-2	0·703976 ± 37
BD11-1	0·704284 ± 41
DA20-1	0·704201 ± 40
DA20-2	0·704165 ± 34
DA20-3	0·704238 ± 68
DA20-4	0·704109 ± 36
DA20-5	0·704238 ± 46
DA20-6	0·704202 ± 46
DA3-1	0·704307 ± 112
DA3-2	0·704304 ± 180
DA1-5	0·704199 ± 40
DA1-6	0·704105 ± 49
DA1-4	0·704125 ± 58
DA1-3	0·704081 ± 35
DA1-2	0·704188 ± 35
DA1-1	0·704429 ± 34
INC43*	0·704127 ± 19
*Matrix**	
LD	0·704266 ± 80
DA	0·704275 ± 21
BD	0·704247 ± 26
INC	0·704254 ± 18

Abbreviations as in Table 1.
*Samples collected by microdrill. Location of analyses is shown in Figs 2 and 6.

ORIGIN OF CRYSTAL POPULATIONS

Plagioclase CSD data for the four compositional products of the 1915 Lassen Peak eruption confirm the presence of three size populations of crystals: phenocrysts, microphenocrysts, and microlites. Our goal is to integrate these results with textural and *in situ* chemical data to further elucidate the origins of these crystal populations and expand on the conclusions made by Clynne (1999).

Unreacted plagioclase phenocrysts

Figure 3 and Table 1 show that phenocrysts from all four compositional products of the 1915 eruption share similar

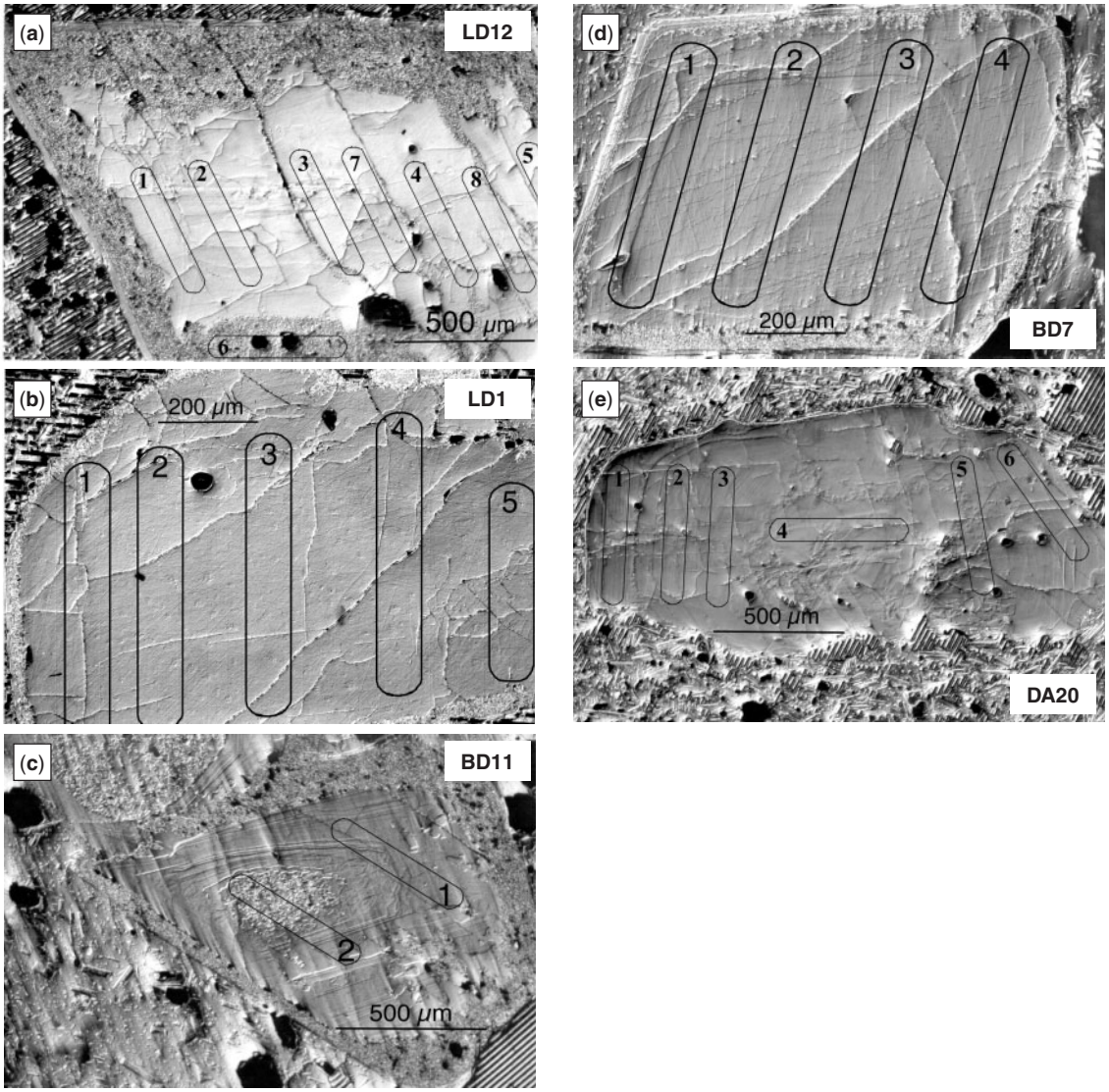

Fig. 8. Nomarski differential interference contrast images of plagioclase analyzed for Sr isotope ratios. Locations of analysis troughs are shown in each image. Number of trough corresponds to analysis number in Table 7.

CSD characteristics. Best-fit linear regression analyses illustrate that, in all four cases, the breaks in slope on the CSD plots occur at similar crystal lengths. In the case of the 3/2 volume correction, phenocrysts are defined as crystals >0·5 mm. This common characteristic suggests that, despite the distinct histories proposed for the four products, all phenocrysts share a common cooling history. Phenocryst CSDs have gentle slopes and low intercepts, suggesting crystallization in an environment characterized by low nucleation rates and small degrees of undercooling (e.g. Marsh, 1988), which implies modest cooling rates (Cashman, 1993). We interpret NDIC images of unreacted phenocrysts, characterized by either smooth textures or pronounced growth zones that are typically parallel to crystal edges, as support for the hypothesis that plagioclase growth was a near-equilibrium process. In contrast to other studies (e.g. Tepley *et al.*, 1999), the general lack of dissolution or other disequilibrium textures recorded in unreacted phenocrysts in this study suggests that prior to the pre-1915 mixing event, mafic recharge was not common during the time period of phenocryst growth.

Major element characteristics of phenocryst cores indicate that this phenocryst population is also chemically distinct. Phenocryst cores have An contents that are distinctly lower than those of microphenocrysts and microlites (Table 1 and Fig. 4) with the notable exception of two cores from the inclusion that show An contents of ~55 and 69 mol % (discussion of these crystals is deferred to a later section). Core-to-rim traverses confirm that compositional

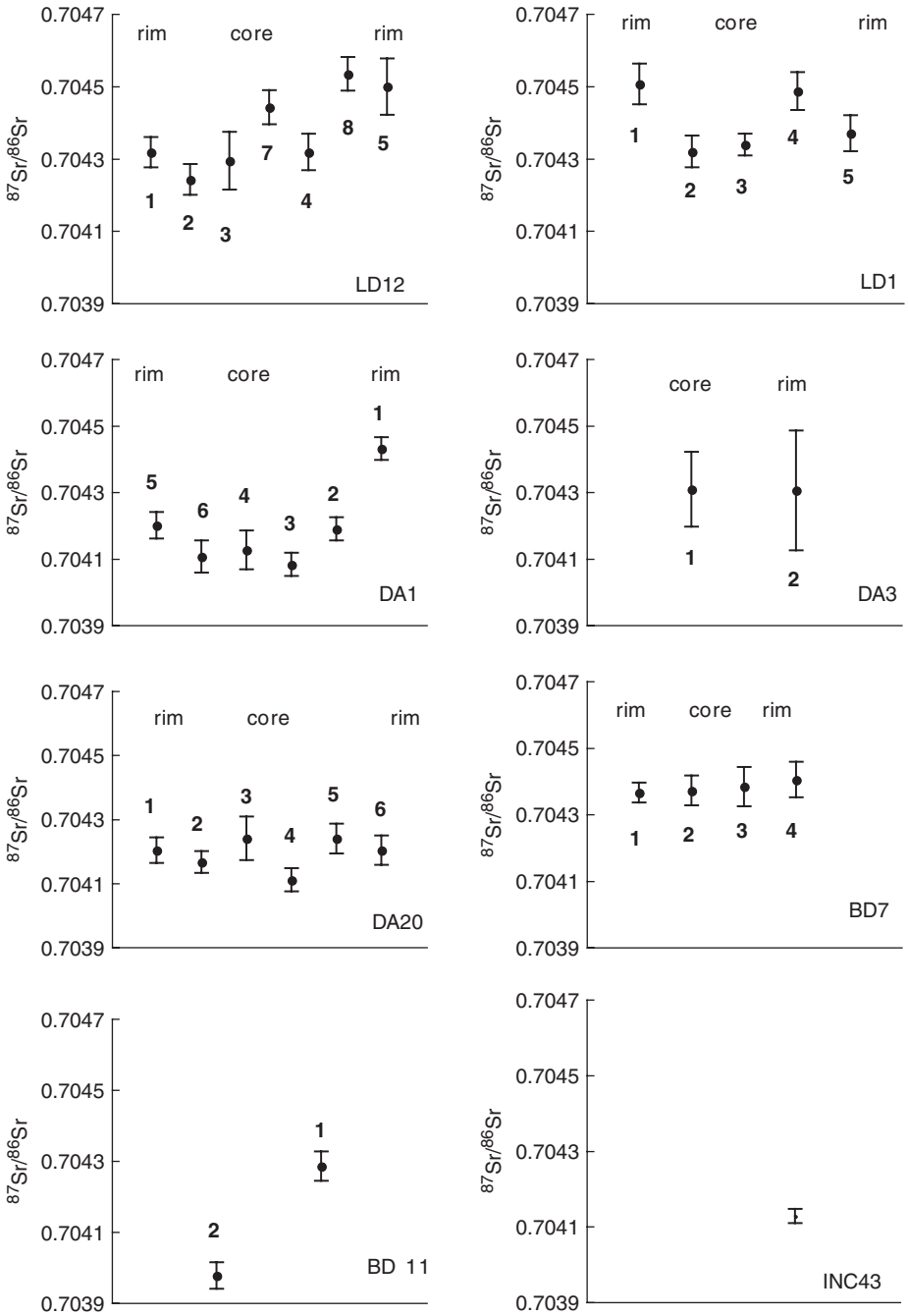

Fig. 9. $^{87}Sr/^{86}Sr$ laser ablation and microdrill data vs relative position in plagioclase crystals. Vertical line associated with each symbol represents analytical uncertainty. Numbers associated with each point correspond to trough numbers from Figs 4 and 8 and Table 7.

zoning within crystals is subtle, with average changes in An over 10–20 μm increments being <1 mol % (Table 5). Dramatic compositional variations are exhibited in some crystals but are not dominant. In addition, it is important to note that a strict correlation between large compositional changes (e.g. ≥6 mol %) and textural discontinuities does not exist. This implies that such compositional changes can occur in the absence of an obvious textural response. The inverse is also the case: textural discontinuities not associated with large compositional changes may be the result of changes in parameters such as temperature, pressure, or water content rather than changes in bulk composition resulting from processes such as magma mixing. Combined textural–chemical studies are, thus, essential for identifying the nature and number of events that affect magma evolution.

Relatively systematic negative correlations between trace elements Pb, Ba, La, Ce, Rb, and Sc and An contents suggest that these elements behaved incompatibly during differentiation. Phenocrysts, which have the lowest An contents of all crystals in the 1915 eruptive products, have the highest trace element concentrations, consistent with such behavior. In contrast, clustering of Y, Nd, Sm, and Eu concentrations over the range of the An contents suggests that these elements were more compatible during differentiation. Sr concentrations of plagioclase phenocrysts are equal to or lower than those of microphenocrysts, suggesting that Sr behaved broadly compatibly, consistent with plagioclase as a fractionating phase. Intracrystal variations of Sr in phenocrysts DA3 and LD8 are small (<6%), consistent with crystals retaining relatively featureless textures (Fig. 4). (Note that for crystal DA3, no trace element analysis was conducted in the mottled zone.) In contrast, Sr variations documented in DA1, which has both major element and textural evidence of non-equilibrium processing, are higher (~13%). Sr isotope variations in phenocrysts are subtle. The average $^{87}Sr/^{86}Sr$ ratio of all phenocrysts is $0{\cdot}70429 \pm 0{\cdot}00013$. Intracrystal variations are minimal, although some texturally complex crystals such as BD11 (which is characterized by a distinct mottled zone) and DA1 (which has several prominent textural discontinuities and variable major element composition) do show variations in $^{87}Sr/^{86}Sr$ greater than analytical uncertainty. In general, the data are broadly consistent with phenocryst growth in a relatively isotopically homogeneous environment.

Together these data indicate that plagioclase phenocrysts grew in a magma body of dacitic composition that was characterized by relatively small degrees of undercooling. Texturally simple crystals grew as minor differentiation took place, as demonstrated by small variations in An content and trace element abundances. With the exception of the proposed mixing event that led to the 1915 eruption, these crystals do not preserve a record of major recharge events. The dominant volume of the dacitic magma body, therefore, can be envisioned as a relatively isolated mass in which thermal energy is being dissipated to the surroundings at a rate consistent with low degrees of undercooling. The lack of pronounced crystal $^{87}Sr/^{86}Sr$ variations (i.e. core to rim) and the lack of substantial variations among phenocrysts suggest that either wallrock assimilation was not a dominant mechanism or, if assimilation was important, that drastic changes in the character and mass of assimilant did not occur during phenocryst growth. This interpretation supports the idea that, at any given time, the Lassen magmatic system consists of a number of smaller, discrete magma bodies, rather than a single magma chamber that periodically experiences recharge events.

Reacted phenocrysts

As demonstrated by CSD results for reacted vs unreacted phenocrysts in the black dacite (Table 1), the thermal environment in which reacted phenocrysts underwent the dominant phase of growth was the same as that for unreacted phenocrysts. We therefore suggest that most of the growth of reacted phenocrysts took place in the pre-mixing dacitic chamber and the disequilibrium textures, of which dusty or mottled zones are the most prominent, formed as a result of the same mixing event that catalyzed the eruption. These crystals also typically have clear overgrowth rims (0·05–0·1 mm thick) with calcic ($An_{54–72}$) compositions similar to that of microphenocrysts. A clear example of a mottled zone surrounded by an overgrowth rim can be seen in Fig. 4e, which shows the NDIC image and electron microprobe traverse for DA3. The association between the mottled zones and the overgrowth rims suggests that mottled zones result from dissolution caused by crystals being entrained in a magma at temperatures higher than those of the dacitic magma (see Tsuchiyama & Takahashi, 1983; Tsuchiyama, 1985). This is consistent with the observation that these mottled zones are composed of small glass inclusions, which form by partial melting of the plagioclase crystals (e.g. Tsuchiyama, 1985). Two Sr isotope analyses of mottled zones vary from 0·70398 (BD11-2) to 0·70431 (DA3-1). The former is lower than the average phenocryst value whereas the latter is very similar; thus, based on this small sampling, there is no clear indication that the dissolution process influenced the Sr isotope systematics. Based on the compositional similarity between the overgrowth rims and microphenocrysts (described below), we agree with the interpretation of Clynne (1999) that growth of the rims occurred concurrently with microphenocryst growth.

Microphenocrysts

Compared with phenocrysts, differences in the slopes of CSD plots (Fig. 3 and Table 1) for microphenocrysts for all four compositions of the 1915 Lassen eruption indicate that these crystals are a distinct population, and like phenocrysts, microphenocrysts share a common origin. Steeper slopes imply higher rates of nucleation associated with higher degrees of undercooling (Marsh, 1988). Acicular, swallowtail, and skeletal textures, common to microphenocrysts, also support growth at high degrees of undercooling (Kirkpatrick *et al.*, 1979; Muncill & Lasaga, 1987).

Like phenocrysts, microphenocrysts also form a compositionally distinct group (Fig. 4 and Table 3). Higher core An contents, compared with phenocrysts, suggest crystallization from a higher temperature, higher CaO magma. Some differentiation during growth of the microphenocrysts took place, as evidenced by generally simple zoning patterns that, on average, trend toward lower An

contents from core to rim (Table 3). These data, combined with crystal textures dominated by growth zones parallel to crystal edges, require a model in which microphenocrysts grew comparatively rapidly in a hybrid magma formed by mixing of the reservoir dacite and intruding basaltic andesite. Rare disequilibrium textures are not typically associated with compositional discontinuities (Table 5), and therefore these textural features may be a consequence of subtle changes in parameters such as temperature or water content rather than major element changes in magma chemistry.

With the exception of the Sr, trace element abundances of microphenocrysts are lower than those of the phenocrysts. Despite differences in temperature and An content of the dacitic and hybrid magmas, which may affect mineral–melt partition coefficients, these concentration differences imply that the dacitic magma was more enriched in these trace elements than the hybrid magma. Bulk-rock trace element analyses (Clynne, 1993; Kernan *et al.*, 2007) support this observation and are consistent with the more mafic nature of the hybrid magma. The behavior of Sr is more complex, as indicated by overlapping concentrations across a wide range of plagioclase An contents (see Fig. 6c). The $^{87}Sr/^{86}Sr$ ratio of a single microphenocryst (0·704127) is lower than the phenocryst average (0·70429) and also lower than the matrix average (0·70426 ± 0·00001). Bullen & Clynne (1990) determined the $^{87}Sr/^{86}Sr$ of the light dacite (=0·70411 ± 0·00003), dark andesite (= 0·70422 ± 0·00003), and inclusion (=0·70421 ±0·00003). Although the *in situ* data suggest that the Sr isotope ratio of the recharge magma was less radiogenic, these whole-rock data suggest a more complicated scenario. Clearly, additional data are required to fully investigate the Sr isotope characteristics of the magma types involved in the eruption.

An interesting result evident from Table 5 is that the contrast between the average core An content of phenocrysts vs microphenocrysts tends to be large (phenocryst cores 34–36 mol %; microphenocryst cores 66–70 mol %). The exceptions are the two phenocrysts from the inclusion that are considered transitional (discussed below). In contrast, rim An contents are much closer to each other (phenocryst rims 47–52 mol %; microphenocryst rims 50–62 mol %). The greatest contrast in rim contents is in plagioclase from the dark andesite.

Plagioclase microphenocryst crystallization was initiated when the hybrid magma layer dropped below the liquidus temperature of plagioclase. CSD and textural data imply higher degrees of undercooling, and thus, faster rates of heat loss from this layer, compared with the dacitic chamber. Phenocrysts caught in the hybrid magma first underwent resorption as a result of exposure to higher temperature, and then experienced rim growth that was in equilibrium with the hybrid magma composition. Differentiation drove the microphenocryst compositions and the rims of the reacted phenocrysts to less An-rich contents, as evidenced by normal zoning in these crystals. The hybrid magma may have had a slightly less radiogenic $^{87}Sr/^{86}Sr$ ratio than its dacitic counterpart, but more work is required to elucidate the isotope characteristics of the end-member magmas. The relatively narrow range of plagioclase microphenocryst compositions and the consistent CSD characteristics for the microphenocryst population imply that the microphenocrysts formed in a magma with minimally variable chemical characteristics, which implies that the mixing that resulted in the hybrid layer was an efficient process across lateral and vertical dimensions.

Transitional crystals

Two crystals classified as phenocrysts based on CSD results have compositions similar to microphenocrysts. These crystals, both found in inclusions (INC8, 520 μm and INC9, 580 μm), have core An contents of 69·3 and 55·4 mol %, respectively. The An content of INC8 is similar to that of microphenocryst cores, whereas the value for INC9 is intermediate between those of microphenocryst and phenocryst cores. Most trace element characteristics for INC9 are also transitional between those of phenocrysts and microphenocrysts (Fig. 6). The exception is the near-rim An content (~69) and trace element characteristics like those of microphenocrysts. This near-rim region is located rimward of a prominent textural discontinuity (Fig. 4g). Thus, the core region of INC9 appears to have transitional characteristics, whereas rimward of the textural discontinuity, the area is characterized by an abrupt increase in An, followed by a decrease. It is possible that the core of this crystal grew during mixing of dacitic and recharge magma, but in proportions slightly different from those associated with typical microphenocrysts. An alternative is that the core represents a rare crystal from a more mafic precursor associated with the reservoir dacite; this possibility seems more likely given the prominent textural discontinuity. The crystal, which would have been in modest disequilibrium with the ambient dacite, underwent resorption in the dacitic chamber. Rim characteristics strongly support a subsequent episode of crystal growth concomitant with microphenocryst formation. INC8 has An core characteristics like those of typical microphenocrysts, suggesting that uncertainty in the division between phenocrysts and microphenocrysts is at least ±20 μm.

Microlites

Distinct changes in slope observed in each CSD plot at 0·1 mm distinguish the third population of plagioclase crystals, defined as microlites. For the light dacite, black dacite, and dark andesite, the absolute values of the slopes are similar (26·7–33·5) and the R^2 values are high (0·94–0·99) (Table 1). Steep slopes imply high nucleation rates, which are interpreted to result from large degrees of

undercooling, caused by rapid magma ascent and syneruptive degassing (e.g. Hammer *et al.*, 2000). We suggest that microlites most probably formed during magma ascent immediately prior to eruption.

In contrast, the absolute value of slope and R^2 (2·6 and 0·33, respectively) for the inclusion microlites are significantly different from those for the other three rock types (Table 1), implying that these crystals grew in an environment distinct from that represented by the black dacite, light dacite, and dark andesite. Based on the model of Clynne (1999), hybrid magma dispersed into the magma chamber as a mafic foam that ascended into the overlying dacite. Inclusions are probably quenched blobs of this material. The high microphenocryst density in the analyzed inclusion suggests that inclusions may have been characterized by comparatively high melt viscosity, which in turn may have retarded microlite growth. Growth on preexisting microphenocrysts, instead of nucleation of new microlites, and/or timescales too short to support formation of a large microlite population are alternatives suggested by the work of Coombs *et al.* (2002).

Microlites form the only crystal population that exhibits a major-element correlation with whole-rock composition. Average microlite core An contents for the black dacite, light dacite, and inclusion are similar (51·7–56·7; Table 3). In contrast, the dark andesite has an average core An content of 63·5 mol %, suggesting crystallization from a more CaO-rich melt. Average rim An contents show that microlites are generally normally zoned, although the higher average An content is still preserved in microlite rims in the dark andesite (61·8 mol % compared with 44·8–48·7 mol % for other products). Results of electron microprobe glass analyses are relevant to this discussion because, of the four compositions, average major-element data indicate that the dark andesite is characterized by the least silicic, most magnesian glass. The preferred model of formation for the dark andesite by Clynne (1999) involves mixing between dacite and mafic end-member magmas. The mafic foam, which formed in a highly undercooled setting following initial mixing, ascended into the main body of dacite. This foam formed inclusions, and disaggregated crystals from the inclusions mixed with the dacite to form the black dacite. As compositional and thermal contrasts between the black dacite and basaltic andesite decreased, direct mixing of these products was possible and formed the dark andesite. The more An-rich microlites and more mafic glass compositions are consistent with this hypothesis. Low thermal contrast between the black dacite and basaltic andesite would retard additional crystal formation, consistent with the observation that the microphenocrysts and phenocrysts present in the dark andesite formed in the andesitic hybrid layer and the dacitic chamber, respectively, and subsequently became part of the dark andesite. Thus, microlites appear to be the only distinct crystal population that formed in the hybrid dark andesite *senso stricto*, and as noted for other microlite populations, probably owe their origin to ascent of magma into the volcanic conduit.

TIMESCALES OF MIXING AND CRYSTALLIZATION PRIOR TO THE 1915 ERUPTION

In this section, timescale information about the three crystal size populations is evaluated. We note that there are assumptions that constrain the applicability of CSD timescales to natural phenomena. Among the most critical is the assumption that during crystal growth, growth and nucleation rates remain constant. An additional uncertainty originates from our imperfect understanding of growth rates, as applied to natural conditions. In all cases, we apply reasonable ranges of growth rates to bracket potential timescales.

Cashman (1993) demonstrated that for plagioclase forming in a shallow magmatic system, growth rates are relatively constant over a wide variety of composition and melt viscosity. The parameter that exerts the most critical control on growth rate is magma cooling rate. Based on comparison of natural and experimental data, in the context of textural and CSD data, Cashman (1993) concluded that growth rates for plagioclase in shallow basaltic systems span a very narrow range of 10^{-9} mm/s to 10^{-10} mm/s. Studies of Mount. St. Helens dome growth by Cashman (1992) show less than an order of magnitude difference in plagioclase growth rates between basaltic and dacitic magmas. Higgins (1996a) used a growth rate of 10^{-10} mm/s to determine CSD-derived residence times of decades for magma in the andesitic crustal chamber beneath Egmont volcano. Using rates of 10^{-9} to 10^{-10} mm/s and the slopes for phenocrysts from both the 3/2 and *CSDCorrections* volume adjustment, average phenocryst residence times [residence time $= -1/(\text{growth rate} \times \text{slope})$] are decades to centuries. Assuming that the maximum measured length of a phenocryst (~5 mm) also provides timescale information, the same range of growth rates yields timescales of centuries to millennia. Similar timescales have been reported from U–Th–Ra disequilibria work for other volcanoes (e.g. Cooper & Reid, 2003; Turner *et al.*, 2003).

A goal of this work is to constrain the time between recharge–mixing and eruption. If microphenocrysts formed in response to magma mixing initiated by recharge, then the average residence time of this crystal population may provide an indication of the time between recharge and eruption. Appropriate growth rates can be estimated based on the work of Coombs *et al.* (2002), which reported results of experiments designed to reproduce crystal textures of inclusions from Southwest Trident volcano, Alaska, that formed in a manner similar to that of

the 1915 Lassen eruption. In Coombs *et al.* (2002), experimental melts of andesite composition were annealed to 1000°C and then cooled to 890°C at different rates from 110°C/h to 2°C/h. Results for 2°C/h experiments most closely approximate the euhedral, slightly elongate plagioclase crystals common to natural enclaves such as those of the 1915 eruption. This cooling rate brackets growth rates from 3×10^{-7} to 6×10^{-8} mm/s based on the empirical calibration curve of Cashman (1993). Such growth rates yield average crystal residence times of days to a few months, implying a relatively short time period between mixing and eruption. These same growth rates yield crystallization times for the 0·05–0·1 mm phenocryst overgrowth rims of days to weeks. Consistent with this result, a maximum crystal size of 0·5 mm yields residence times of up to several months. Similar timescales were calculated by Nakamura (1995) for the 1991–1993 eruptions of Unzen, based on diffusion modeling of zoning profiles in magnetite formed by mixing low-temperature, crystal-rich magma with a higher temperature melt. Relatively short timescales between mixing and eruption were also proposed for the 1991 eruption of Pinatubo (Pallister *et al.*, 1992), the 1995–1999 eruption of Soufrière Hills, Montserrat (Murphy *et al.*, 2000), and the 1953–1974 eruption of Southwest Trident volcano, Alaska (Coombs *et al.*, 2000).

An interesting observation relevant to this discussion is that phreatic eruptions at Lassen predated the magmatic eruption by nearly a year (Clynne *et al.*, 1999). Pallister *et al.* (1996) speculated that the initial phreatic eruptions of Mt. Pinatubo in 1991 coincided with initial, slow mixing between intruding basaltic and reservoir magma that led to the eruption of inclusion-rich lava 2 months later. The climactic, plinian eruption followed 2 weeks later and is thought to have been triggered by a larger, more efficient mixing event. If magma recharge triggered the onset of phreatic activity at Lassen Peak, then the calculated residence times of the microphenocrysts are significantly shorter than the time between such a recharge event and eruption. A potential explanation for the mismatch in timescales comes from evaluation of the Coombs *et al.* (2002) experiments; they noted that significant crystallization occurred in less than an hour during cooling experiments that attempted to recreate andesite and dacite interaction. Coombs et al. concluded that an intruding andesitic magma cannot be in prolonged contact with a dacitic magma without crystallization occurring. If this is the case, then it is likely that crystallization of microphenocrysts occurred shortly after mixing. Thus, crystallization in this environment may have occurred relatively quickly, and then may have slowed significantly or stopped as a result of thermal equilibration between host and intruding magma (e.g. Sparks & Marshall, 1986). If crystallization were discontinuous, then the calculated CSD timescales represent a lower limit on the time between mixing and recharge. A less likely, but alternativee interpretation is that the timescale implied by our CSD data is accurate. This would suggest that phreatic activity was not directly initiated by the recharge event that is represented by the microphenocryst population. Thus, a key question for the 1915 Lassen Peak eruption is how recharge and the onset of phreatic activity are related.

More rapid cooling rates of 10°C/h yield growth rates of 1×10^{-6} to 2×10^{-7} mm/s based on the empirical calibration curve of Cashman (1993). This range encompasses the average microlite growth rate for the 1991 eruption of Mt. Pinatubo of 1×10^{-7} mm/s (Cashman & Blundy, 2000). If this range is appropriate for the 1915 microlite population, residence times are of the order of hours to days. Calculations using the maximum crystal size (0·1 mm) also yield timescales of hours to days. Based on an analysis of microlite crystallinity for samples representing activity during the 1991 eruption of Mt. Pinatubo, Hammer *et al.* (1999) proposed similar, short timescales for microlite growth. Blundy & Cashman (2005) also proposed short timescales (i.e. months) for crystal growth, based on constraints provided by melt inclusions from 1980 Mount St. Helens dacitic pumice. Such rapid timescales may preclude crystallization caused by dissipation of latent heat. Instead, syn-eruptive degassing and decompression cause crystallization on relatively short timescales (e.g. Hammer *et al.*, 1999, 2000; Cashman & Blundy, 2000). We therefore suggest that microlite crystallization in the Lassen system was associated with decompression and syn-eruptive degassing as the magma ascended in a conduit system to the surface.

SUMMARY: PROCESSES AND TIMESCALES OF THE MAGMA MIXING EVENT ASSOCIATED WITH THE 1915 LASSEN PEAK ERUPTION

Phenocrysts in all of the products from the 1915 Lassen Peak eruption provide evidence for the existence of a relatively isolated dacitic magma body that was undergoing moderate rates of cooling. Simple textures, relatively homogeneous Sr isotope signatures, and small variations in trace element concentrations and An content indicate that the dacitic magma underwent only modest, closed-system differentiation prior to the eruption-inducing mixing event. If assimilation occurred, the mass and character of assimilant was constant during crystallization. Average crystal residence times record crystallization over hundreds to thousands of years.

Months prior to the climactic 1915 eruption, basaltic andesite intruded into the base of the dacitic reservoir. As a hybrid layer of andesite formed, microphenocrysts of plagioclase crystallized. Textural and CSD data indicate a

higher degree of undercooling for this layer, compared with the reservoir chamber, suggesting more rapid rates of heat dissipation. Microphenocryst cores have higher An contents than phenocryst cores and are also characterized by lower concentrations of incompatible elements such as Ba and Pb. Combined CSD and *in situ* chemical data therefore determine microphenocrysts to be a distinct population. Some phenocrysts were incorporated into the hybrid layer, exposing them to higher temperature, higher CaO magma, causing some resorption, followed by the formation of overgrowth rims. These rims, as well as the rims of the microphenocrysts, are typically normally zoned, suggesting that after the formation of the relatively high An content portions, differentiation by crystallization led to reduced An content in the remaining hybrid magma.

Crystallization of the hybrid layer led to volatile saturation, which induced vesiculation of the hybrid magma. A mafic foam formed, which was less dense than the ambient dacitic reservoir magma, and rose within the chamber. Inclusions represent discrete blobs of this material incorporated into the black dacite. There is also abundant evidence that some inclusions disaggregated, as indicated by the presence of comparable microphenocrysts in the light dacite, black dacite, and dark andesite.

Microlite CSD data suggest short residence times of hours to days, which most probably reflect decompression–degassing during ascent in the magma conduit system. Growth of microlites in the inclusions was distinct from that in the magmas that formed the other three rock types. The much higher microphenocryst abundance in the inclusions may have influenced magma rheology, thus retarding growth of microlites. An alternative is that some of the plagioclase growth that occurred during this phase did so on pre-existing microphenocrysts. Compositional distinctions in microlites and glass between black dacite, light dacite, inclusion, and dark andesite clearly demonstrate microlite growth after formation of the mafic foam and dispersal of the inclusions into the reservoir magma. The melt composition of the dark andesite was more mafic than that of the other compositions, reflecting mixing between black dacite and intruding basaltic andesite on timescales so short that little new (pre-microlite) crystallization occurred. Although the average composition of the andesitic inclusion is more mafic than that of the dark andesite, by the time the microlites began to grow, the melt composition of the inclusions had evolved to a composition similar to that of the black dacite and light dacite.

ACKNOWLEDGEMENTS

We thank Roger Nielsen and Frank Tepley for assistance with microprobe analyses at Oregon State University, Martin Streck for use of his Nomarski imaging facility at Portland State University, and Darren Tollstrup for assistance with laser ablation and microdrilling. Thoughtful reviews by Michelle Coombs, Pavel Izbekov, Dougal Jerram, Carl Thornber and Charles Bacon, and expert handling by executive editor Marjorie Wilson are greatly appreciated. The authors gratefully acknowledge funding from the National Science Foundation, Sigma Xi, Geological Society of America, and Central Washington University.

SUPPLEMENTARY DATA

Supplementary data for this paper are available at *Journal of Petrology* online.

REFERENCES

Anderson, A. T. (1983). Oscillatory zoning of plagioclase: Nomarski interference contrast microscopy of etched polished sections. *American Mineralogist* **68**, 125–129.

Bacon, C. R. (1986). Magmatic inclusions in silicic and intermediate volcanic rocks. *Journal of Geophysical Research* **91**, 6091–6112.

Blundy, J. & Cashman, K. V. (2005). Rapid decompression-driven crystallization recorded by melt inclusions from Mount St. Helens volcano. *Geology* **33**, 793–796.

Browne, B. L., Vogel, T. A., Uto, K., Hoshizumi, H., Eichelberger, J. C. & Patino, L. C. (2006). Magma mingling as indicated by texture and Sr/Ba ratios of plagioclase phenocrysts from Unzen volcano, SW Japan. *Journal of Volcanology and Geothermal Research* **154**, 103–116.

Bullen, T. D. & Clynne, M. A. (1990). Trace element and isotopic constraints on magmatic evolution at Lassen volcanic center. *Journal of Geophysical Research* **95**, 19671–19691.

Cashman, K. V. (1990). Textural constraints on the kinetics of crystallization of igneous rocks. In: Nicholls, J. & Russell, J. K. (eds) *Modern Methods of Igneous Petrology: Understanding Magmatic Processes. Mineralogical Society of America, Reviews in Mineralogy* **24**, 259–314.

Cashman, K. V. (1992). Groundmass crystallization of Mount St. Helens dacite, 1980–1986: a tool for interpreting shallow magmatic processes. *Contributions to Mineralogy and Petrology* **109**, 431–449.

Cashman, K. V. (1993). Relationship between plagioclase crystallization and cooling rate in basaltic melts. *Contributions to Mineralogy and Petrology* **113**, 126–142.

Cashman, K. V. & Blundy, J. (2000). Degassing and crystallization of ascending andesite and dacite. *Philosophical Transactions of the Royal Society of London* **358**, 1487–1513.

Cashman, K. V. & Marsh, B. D. (1988). Crystal size distribution (CSD) in rocks and the kinetics and dynamics of crystallization II: Makaopuhi lava lake. *Contributions to Mineralogy and Petrology* **99**, 292–305.

Christiansen, R.L., Clynne, M.A. & Muffler, L.J.P. (2002). Geologic map of the area of Lassen Peak, Chaos Crags, and Upper Hat Creek, California. *US Geological Survey Miscellaneous Investigations Map* **I–2723**, scale 1:50 000.

Clynne, M. A. (1990). Stratigraphic, lithologic, and major element geochemical constraints on magmatic evolution at Lassen volcanic center, California. *Journal of Geophysical Research* **95.**

Clynne, M. A. (1993). Geologic studies of the Lassen volcanic center, Cascade Range, California. PhD thesis. University of California, Santa Cruz.

Clynne, M. A. (1999). A complex magma mixing origin for rocks erupted in 1915, Lassen Peak, California. *Journal of Petrology* **40**, 105–132.

Clynne, M. A., Christiansen, R. L., Felger, T. J., Stauffer, P. H. & Hendley, J. W., II (1999). Eruptions of Lassen Peak, California, 1914–1917. *US Geological Survey Fact Sheet*, 173–98.

Coombs, M. L., Eichelberger, J. C. & Rutherford, M. J. (2000). Magma storage and mixing conditions for the 1953–1974 eruptions of Southwest Trident volcano, Katmai National Park, Alaska. *Contributions to Mineralogy and Petrology* **140**, 99–118.

Coombs, M. L., Eichelberger, J. C. & Rutherford, M. J. (2002). Experimental and textural constraints on mafic enclave formation in volcanic rocks. *Journal of Volcanology and Geothermal Research* **119**, 125–144.

Cooper, K. M. & Reid, M. R. (2003). Re-examination of crystal ages in recent Mount St. Helens lavas: Implications for magma reservoir processes. *Earth and Planetary Science Letters* **213**, 149–167.

Eggins, S. M. (2003). Laser ablation ICP-MS analysis of geological materials prepared as lithium borate glasses. *Journal of Geostandards and Geoanalyses* **27**, 147–162.

Eichelberger, J. C. (1980). Vesiculation of mafic magma during replenishment of silicic magma reservoirs. *Nature* **288**, 446–450.

Garrido, C. J., Kelemen, P. B. & Hirth, G. (2001). Variation of cooling rate with depth in lower crust formed at an oceanic spreading ridge: Plagioclase crystal size distributions in gabbros from the Oman ophiolite. *Geochemistry, Geophysics, Geosystems* **2**, doi:10.1029/2000GC000136.

Guffanti, M., Bullen, T. D., Clynne, M. A., Smith, J. G. & Muffler, L. J. P. (1990). Late Cenozoic volcanism, subduction, and extension in the Lassen region of California, southern Cascade Range. *Journal of Geophysical Research* **95**, 19453–19464.

Hammer, J. E., Cashman, K. V., Hoblitt, R. P. & Newman, S. (1999). Degassing and microlite crystallization during pre-climactic events of the 1991 eruption of Mt. Pinatubo, Philippines. *Bulletin of Volcanology* **60**, 355–380.

Hammer, J. E., Cashman, K. V. & Voight, B. (2000). Magmatic processes revealed by textural and compositional trends in Merapi dome lavas. *Journal of Volcanology and Geothermal Research* **100**, 165–192.

Higgins, M. D. (1996*a*). Crystal size distributions and other quantitative textural measurements in lavas and tuff from Egmont volcano (Mt. Taranaki), New Zealand. *Bulletin of Volcanology* **58**, 194–204.

Higgins, M. D. (1996*b*). Magma dynamics beneath Kameni volcano, Thera, Greece, as revealed by crystal size and shape measurements. *Journal of Volcanology and Geothermal Research* **70**, 37–48.

Higgins, M. D. (2000). Measurement of crystal size distributions. *American Mineralogist* **85**, 1105–1116.

Higgins, M. D. (2006). Verification of ideal semi-logarithmic, lognormal or fractal crystal size distributions from 2D datasets. *Journal of Volcanology and Geothermal Research* **154**, 8–16.

Izbekov, P. E., Eichelberger, J. C. & Ivanov, B. V. (2004). The 1996 eruption of Karymsky volcano, Kamchatka: Historical record of basaltic replenishment of an andesite reservoir. *Journal of Petrology* **45**, 2325–2345.

Kernan, R. A., Wenner, J. M., Clynne, M. A., Mahoney, J. B. & Ferguson, J. W. (2007). Dynamic magma chamber processes reflected in trace-element data from the May 1915 eruption of Lassen Peak, California (abstract). *EOS Transactions, American Geophysical Union* **88**, Fall Meeting Supplement, Abstract V33C-1522.

Kirkpatrick, R. J., Klein, L., Uhlmann, D. R. & Hays, J. F. (1979). Rates and processes of crystal growth in the system anorthite–albite. *Journal of Geophysical Research* **84**, 3671–3676.

Mangan, M. T. (1990). Crystal size distribution systematics and the determination of magma storage times: the 1959 eruption of Kilauea volcano, Hawaii. *Journal of Volcanology and Geothermal Research* **44**, 295–302.

Marsh, B. D. (1988). Crystal size distribution (CSD) in rocks and the kinetics and dynamics of crystallization I. Theory. *Contributions to Mineralogy and Petrology* **99**, 277–291.

Marsh, B. D. (1998). On the interpretation of crystal size distributions in magmatic systems. *Journal of Petrology* **39**, 553–600.

Morgan, D. J. & Jerram, D. A. (2006). On estimating crystal shape for crystal size distribution analysis. *Journal of Volcanology and Geothermal Research* **154**, 1–7.

Muncill, G. E. & Lasaga, A. C. (1987). Crystal-growth kinetics of plagioclase in igneous systems: one-atmosphere experiments and application of a simplified growth model. *American Mineralogist* **72**, 299–311.

Murphy, M. D., Brewer, T. S., Sparks, R. S. J., Barclay, J. & Carrol, M. R. (2000). Remobilization of andesite magma by intrusion of mafic magma at the Soufrière Hills volcano, Montserrat, West Indies. *Journal of Petrology* **41**, 21–42.

Nakamura, M. (1995). Continuous mixing of crystal mush and replenished magma in the ongoing Unzen eruption. *Geology* **23**, 807–810.

Pallister, J. S., Hoblitt, R. P. & Reyes, A. G. (1992). A basalt trigger for the 1991 eruptions of Pinatubo volcano? *Nature* **356**, 426–428.

Pallister, J. S., Hoblitt, R. P., Meeker, G. P., Knight, R. J. & Siems, D. F. (1996). Magma mixing at Mount Pinatubo: Petrographic and chemical evidence from the 1991 deposits. In: Newhall, C. G. & Punongbayan, R. S. (eds) *Fire and Mud: Eruptions and Lahars of Mt. Pinatubo, Philippines*. Seattle, WA, University of Washington Press, pp. 687–732.

Pearce, T. H. & Clark, A. H. (1989). Nomarski interference contrast observations of textural details in volcanic rocks. *Geology* **17**, 757–759.

Pearce, T. H. & Kolisnik, A. M. (1990). Observations of plagioclase zoning using interference imaging. *Earth-Science Reviews* **29**, 9–26.

Ramos, F.C. (1992). Isotope geology of the Grouse Creek Mountains, Box Elder county Utah, MS thesis, University of California Los Angeles, Los Angeles.

Ramos, F. C., Wolff, J. A. & Tollstrup, D. L. (2004). Measuring $^{87}Sr/^{86}Sr$ variations in minerals and groundmass from basalts using LA-MC-ICPMS. *Chemical Geology* **211**, 135–158.

Randolf, A. D. & Larson, M. A. (1971). *Theory of Particulate Processes*. New York, Academic Press.

Resmini, R. G. & Marsh, B. D. (1995). Steady-state volcanism, paleoeffusion rates, and magma system volume inferred from plagioclase crystal size distributions in mafic lavas: Dome Mountain, Nevada. *Journal of Volcanology and Geothermal Research* **68**, 273–296.

Salisbury, M. J. (2003). Magma mixing histories recorded by plagioclase crystals from the 1915 eruption of Lassen Peak, California. MS thesis. Central Washington University, Ellensburg.

Singer, B. S., Dungan, M. A. & Layne, G. D. (1995). Textures and Sr, Ba, Mg, Fe, K, and Ti compositional profiles in volcanic plagioclase: clues to the dynamics of calc-alkaline magma chambers. *American Mineralogist* **80**, 776–798.

Sparks, R. S. J. & Marshall, L. A. (1986). Thermal and mechanical constraints on mixing between mafic and silicic magmas. *Journal of Volcanology and Geothermal Research* **29**, 99–124.

Tepley, F. J., III, Davidson, J. P. & Clynne, M. A. (1999). Magmatic interactions as recorded in plagioclase phenocrysts of Chaos Crags, Lassen Volcanic Center, California. *Journal of Petrology* **40**, 787–806.

Thomas, N. & Tait, S. R. (1997). The dimensions of magmatic inclusions as a constraint on the physical mechanism of mixing. *Journal of Volcanology and Geothermal Research* **75**, 167–178.

Tsuchiyama, A. (1985). Dissolution kinetics of plagioclase in the melt of the system: diopside–albite–anorthite, and origin of

dusty plagioclase in andesites. *Contributions to Mineralogy and Petrology* **89**, 1–16.

Tsuchiyama, A. & Takahashi, E. (1983). Melting kinetics of a plagioclase feldspar. *Contributions to Mineralogy and Petrology* **84**, 345–354.

Turner, S., Hawkesworth, C., George, R., Jerram, D. A. & Carpenter, N. (2003). Case studies of plagioclase growth and residence times in island arc lavas from Tonga and the Lesser Antilles, and a model to reconcile discordant age information. *Earth and Planetary Science Letters* **214**, 279–294.

Turrin, B. D., Gerstel, W. J., Muffler, L. J. P., Trimble, D. A., Christiansen, R. L., Clynne, M. A. & Champion, D. E. (1998). Age of Lassen Peak, California, and implications for the ages of late Pleistocene glaciations in the southern Cascade Range. *Geological Society of America Bulletin* **110**, 931–945.